Chapter 8

Intensity maps

Contents

In order to characterize the global geometry, the inhomogenities, the surface intensity contrast of RSGs, the RHD simulations must be compared to the interferometric data at different wavelengths. In this direction, a first step consists in the computation of intensity maps with OPTIM3D and in the calculation of the corresponding visibility curves and phases. Then, I will provide a series of predictions about the visibility curves and phases. At the end, I will compare these prediction with some interferometric observations of RSGs.

8.1 The code for computing visibility curves and phases from the intensity maps

I developed a code (Appendix E) based on the IDL data visualization and analysis platform
(http://www.ittvis.com/idl/) for the visibility and phase computation.
The code basically reads a FITS file. This file is a model that can be a two-dimensional UD or LD models or RHD intensity maps. In the file header the wavelength and the size of the image must be provided: only squared images can be processed.
Then, a Fast Fourier Transform algorithm is applied to the intensity maps resulting from OPTIM3D.

The FFT returns a complex array that has the same dimension of the input image. The storage scheme of the FFT process in IDL follows the outline presented in Fig. 8.1 (from black to red numbers, the data block 2 does not move). Along one dimension, the resulting function is stored in the order associated with the following values of N interval: 0,1,2,...,N/2,-(N/2-1),-(N/2-1),...,-1, in a range [0, T] where T is the period. Thus, it is necessary to shift the zero frequency location from (0, 0) to the center of the display (green numbers in the Figure), in a range [-T/2, T/2].

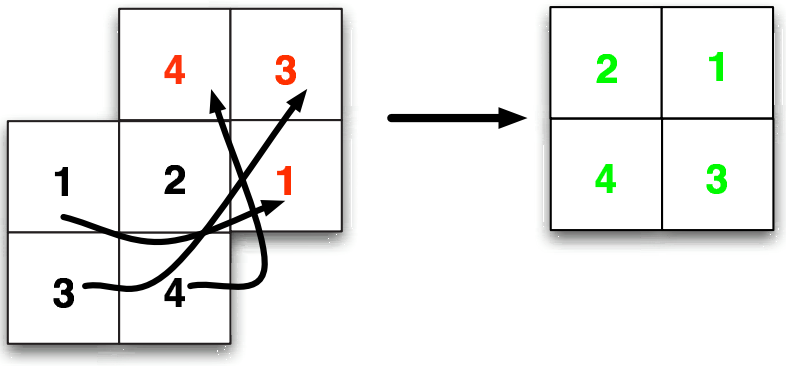

Figure 8.1: Outline of the FFT algorithm output in IDL. The black number correspond to four data-blocks of the original two-dimensional image, then the red number shows the swap due to the FFT algorithm. A final shift of the data-blocks is necessary (green).

Before computing the visibilities, two parameters are important: (i) the wavelength

that is read in the FITS file header; (ii) the pixsize that is the number of pixel per seconds of arc. I use the former to convert the cylces/" into meters; the latter determines the stellar radius θ (in second of arc) at a certain distance (in parsec) using the radius $R_\star$ defined as in Sect. 4.2 (in cm):

$$\theta = \frac{R_\star \cdot \text{pixsize}\cdot}{\text{deltaX}} \tag{8.1}$$

$$d = \frac{\text{deltaX}}{\text{pixsize} \cdot AU} \tag{8.2}$$

where deltaX is the size in cm of the RHD model grid point ($0.6022097 \cdot 10^{12}$ cm for the simulation used in this part of the work) and AU is the astronomical unit.
Basically, the code follows these steps:

1. the FFT is computed for the image
2. the resulting FFT can be rotated
3. visibility and phases are computed considering different cuts in the Fourier Plane. The resulting visibilities depend on the number of pixel per seconds of arc that is set by hand because this implies that I have scaled the simulation at a certain distance
4. the output is written under IDL-save format

The code can be used to create observables directly comparable to observations in term of visibility curves and phases. Moreover, it is also possible to simulate the visibility/phase points detected by all the configurations of VLTI-AMBER thanks to F. Millour who provided me with some routines written in yorick (http://yorick.sourceforge.net/index.php) of VLTI data reduction package that I adapted to IDL.

8.1.1 Test - visibility curve of a uniform disk

I have tested the computed visibility with the simple case of a uniform disk. For this purpose, I generated a UD image (i.e., an image where all the points are set to zero but in the center there are few points equal to 1) and i checked if the visibility curves computed with the code described above correspond to the ones calculated analytically from Eq. 7.14.
Fig. 8.2 displays that the differences are visible at the null points: the analytical solution (black) is more precise than the UD image (red dashed line). This is due to the UD image finite size in the Fourier plan.
Moreover, since FT always treats an image as if it were part of a periodically replicated array of identical images extending horizontally and vertically to infinity, there are strong edge effects between the neighbors of such a periodic array. In order to reduce the problems due to the finite size of the object and to avoid the edge effects, the resolution in the Fourier plane is increased by padding with zero points the input image (usually from 95x95 to 315x315, depending on the RHD model resolution). I found that the best resolution versus CPU-time compromise is 2048x2048 points.

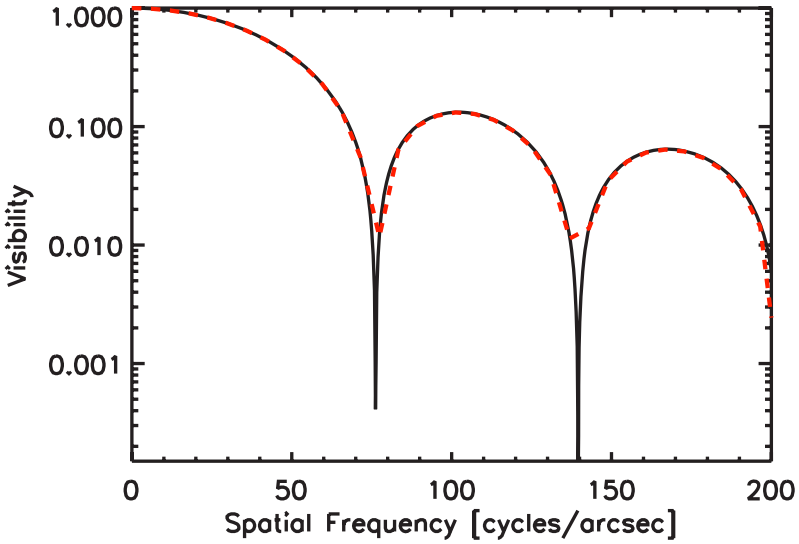

Figure 8.2: Visibility of a uniform disk of 16 mas obtained from Eq. 7.14 (solid black line) is compared to the visibility of a UD (red dashed line) computed with the code described in the text.

8.1.2 Test - closure phase of a uniform disk

The computation of the phases is a difficult task with IDL. First, the edge effects described in the previous section affect also the phases. The image must be dimensioned to at least 6656x6656 points (this size is limited by the IDL-32 bit memory on macintosh computers). In addition, the FFT phases derived by the IDL FFT algorithm show large

"artificial" oscillations especially for non-circular symmetric sources. I corrected it by multiplying each i, j points in the uv-plane with $(-1)^{(i+j)}$ (A. Isella private communication). The reason is the following: the FFT output is shifted of half side of the image (see Fig. 8.1), computing FFT$\left(\text{image}_{\text{i,j}} \cdot (-1)^{(\text{i+j})}\right)$ one obtains the non-shifted transformation. This problem is a numerical problem and depends on the FFT algorithm that is used. There is the FFTW library[14] that should reduce the oscillations (A. Isella private communication). I have started using IDL because of the visualization is also important, however, I have planned to implement a better FFT algorithm to solve this problem.
For the present work, I have used the IDL FFT library corrected as described above and Fig. 8.3 shows how the closure phase of a UD behaves with the resolution in the Fourier plan. As reported in Sect. 7.4.2, the closure phase of a UD have to be 0° or 180°. It is clear from the Figure that this condition is not matched, and that resizing the input image is crucial to obtain values closer to the expected ones. At 200 m, the closure phases is about 10% larger than what is expected, even for a box $\sim$ 35 times larger the object size.
The calculations reported in this work have been done using the highest resolution available and applying the correction to the oscillation.

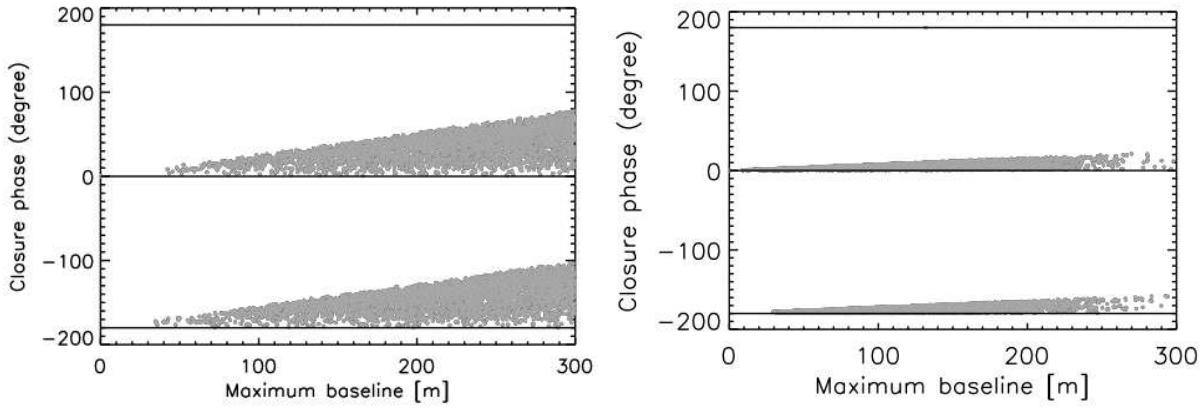

Figure 8.3: Scatter plot of closure phases of 20000 random triangles with a maximum linear extension of 300m as a function of their maximum side. *Left panel*: uniform disk of 16 mas (0.082 pixel per mas), the image has been dimensioned to 2048x2048 points. *Right panel*: same UD with the dimensions increased to 6656x6656 points to reduce edge effects.

8.2 Maps in the transmission filters

In this work, the polychromatic intensity maps presented have been computed using two transmission filters. In the H band, IONIC (Integrated Optics Near-infrared Interferometric Camera; Berger et al. 2003) and in the K band, FLUOR (Fiber Linked Unit for Optical Recombination; Coude Du Foresto et al. 1998) filters mounted at IOTA (Traub et al. 2003). The spectral resolution for the calculation is R=50000. I have tested that

[14] http://www.fftw.org/

this resolution gives a good description of the intensity maps and the resulting visibility curves do not change increasing the spectral resolution.

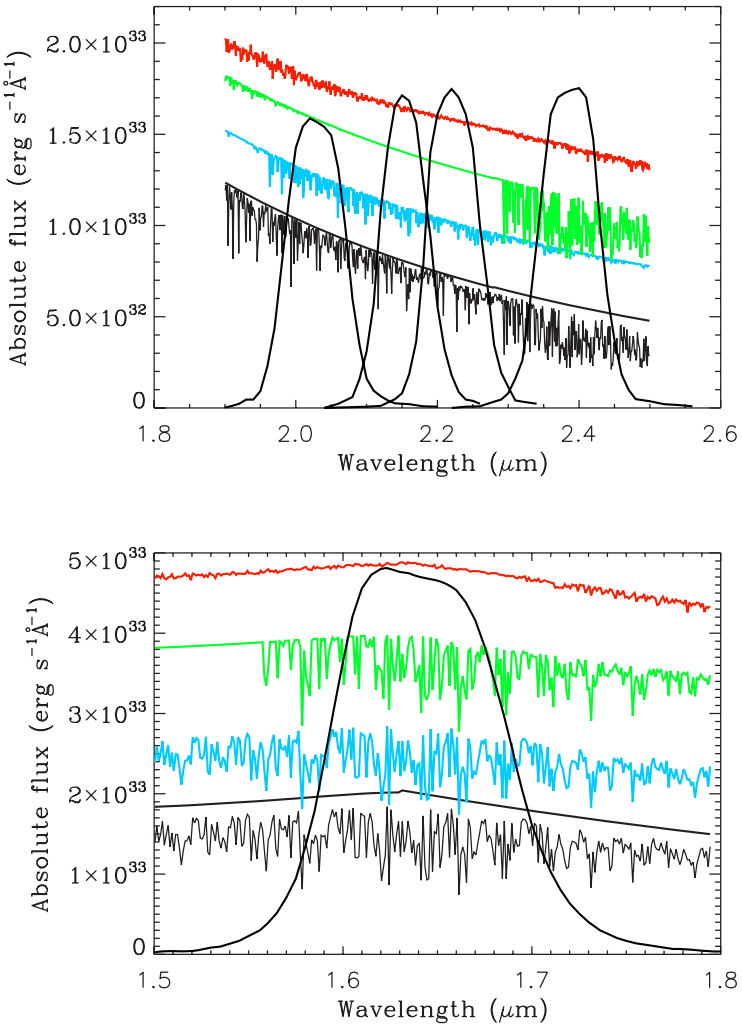

Figure 8.4: *Top panel:* the transmission curves of the 4 narrow band filters mounted on FLUOR instrument at IOTA together with the K band synthetic spectrum with the continuum (bottom black curve) of a RSG computed from the best model available st35gm03n07 in Tab. 4.1. From the top (an offset is applied to these curves, $0.9*10^{33}$, $0.6*10^{33}$ and $0.3*10^{33}$ erg/cm^2/s/Å, respectively), the computed spectra for only H_2O (red), CO bands(green), CN (blue). For cool late-type stars, the K203 filter probes CN bands, while K239 probes CO (H_2O has a small contribution). K215 and K222 are centered on the K-continuum. *Bottom panel:* the transmission curve of the filter mounted on IONIC at IOTA together with the H band synthetic spectrum with the continuum (bottom black curve) of a RSG computed with the same RHD model. From the top (an offset is applied to these curves, $3*10^{33}$, $2*10^{33}$ and $1*10^{33}$ erg/cm^2/s/Å, respectively), the first red curve is H_2O only, then the green one corresponds to a CO only synthetic spectrum and the blue one shows the CN bands.

The K band filters are: K203 (central wavelength is 2.03 μm), K215 (central wavelength is 2.15 μm), K222 (central wavelength is 2.2 μm) and K239 (central wavelength is 2.39 μm). The two continuum filters are K215 and K222 sample the maximum transition region of the K band. While K203 (CN bands and water) and K239 (CO bands) sample the edge of the band (Fig. 8.4, top panel).
The H band filter has a central wavelength at 1.64 μm (same Figure, bottom panel). In this filter, there are a number of CO bands contributing.

Table 8.1: Band filter characteristics and interferometric coupler splitting ratios as measured in laboratory calibrations (for FLUOR K band filters see Perrin et al. 2004b)

Filter	λ_{center} (μm)	FWHM (μm)	R	T
IONIC	1.64	0.10	-	-
K203	2.03	0.10	0.67	0.33
K215	2.15	0.10	0.53	0.47
K222	2.22	0.10	0.56	0.44
K239	2.39	0.10	0.78	0.22

8.3 Limb darkening law

8.3.1 Intensity profiles

The RHD simulation used in this part of the work is st35gm03n07 in Tab. 4.1. If other simulations have been processed, they are indicated in the text.

Two intensity maps computed in IONIC and K222 (K band continuum) filters are shown in Fig. 8.5 (the temporal sequence of st25gm03n07 is displayed in Fig. 4.7). In next section, I will compute the limb darkening fit using these two filters and in this section I want to point out some important uncertainties on the spatial and temporal fluctuations of the intensity profiles.

From Fig. 8.5 (see also Sect. 4.7), it seems that the structure contrast in the IONIC filter is more visible than in the K222 filter. The contrast of the bright structures with respect to the dark ones is a little stronger in the H band than in the K band.

I shall define the impact parameter, p, as the perpendicular distance of a ray from a parallel ray passing through the center of the star. The total flux of the star (Mihalas 1978) is

$$F = 2\pi \int_0^\infty \mathrm{I\,(p)\,pdp} \tag{8.3}$$

where $\mathrm{R}_\star$ is the stellar radius (defines as in Sect. 4.2), $\mathrm{I\,(p)}$ is the intensity emerging along the ray with impact parameter p. The contribution to the flux of the star is reported in Fig. 8.6 (top row) for one snapshot (the same as in Fig. 8.5) in the IONIC and K222

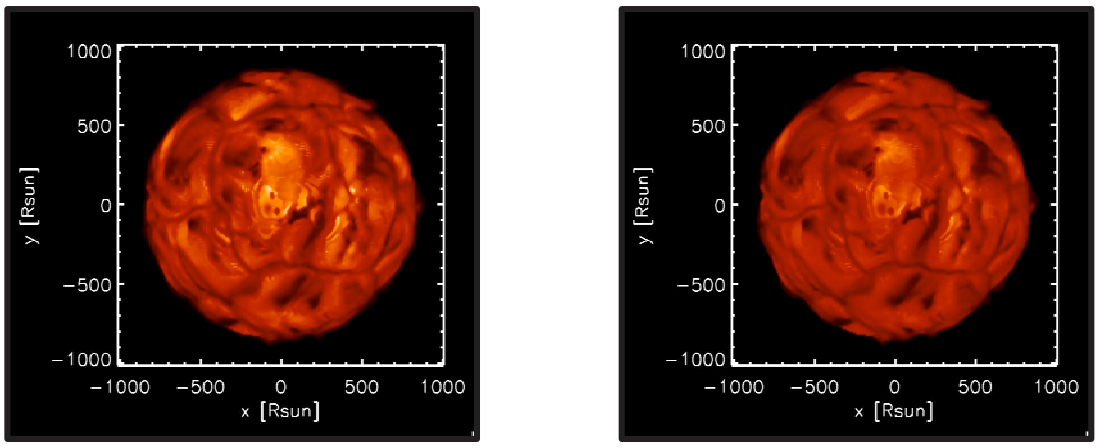

Figure 8.5: Maps of the linear intensity in the IONIC filter (left panel; a scale is used within the range [0,310000] erg/s/cm^2/Å) and in the continuum K222 filter (right panel, [0,150000] erg/s/cm^2/Å). The stellar parameters of this snapshot are: L = 96675 $L_\odot$, R = 842 $R_\odot$, T = 3506K and log(g) = -0.35.

filters.
This quantity shows at what radius the contribution to the flux is important: the region around radius equal to 1 is the most important while at the stellar limb (radius/$R_\star$ ∼1.02) and at the disk center (radius/$R_\star$ ∼0.3), the flux is already factor 10 lower.
In the same Fig. 8.6 (always top row), I can see clearly that the intensity fluctuations at one sigma (blue line) and two sigma (yellow line) around the average profile (red line) are quite strong. In order to quantify them, in the bottom row of Fig. 8.6, I display the spatial fluctuations of the intensity at one sigma for different snapshots as a function of the radius (the interval covered is 3.5 years). In the H band (bottom left panel), the dispersion is much stronger than in the K band (bottom right panel). The average value over time is $\sim 30-35\%$ for IONIC filter and $\sim 25-30\%$ for K222. The different surface structures seen in Fig. 8.5 affect strongly the intensity distribution and intensity dispersion in H and K bands.

In Fig. 8.7, I show the angular intesity dispersion for a typical snapshot (top row) and the temporal intensity dispersion (bottom row) as a function of the radius (normalized to the radius of the star, $R_\star$ define as in Sect. 4.2). The radius corresponds to the impact parameter p defined above. For the temporal fluctuations, I have averaged the radial intensity for each snapshot in the IONIC and K222 filters. In this Figure, the intensity is not a growing function because it is not multiplied by the impact parameter.
The temporal interval covered is 3.5 years. The angular dispersion is larger than the temporal one in both filters.

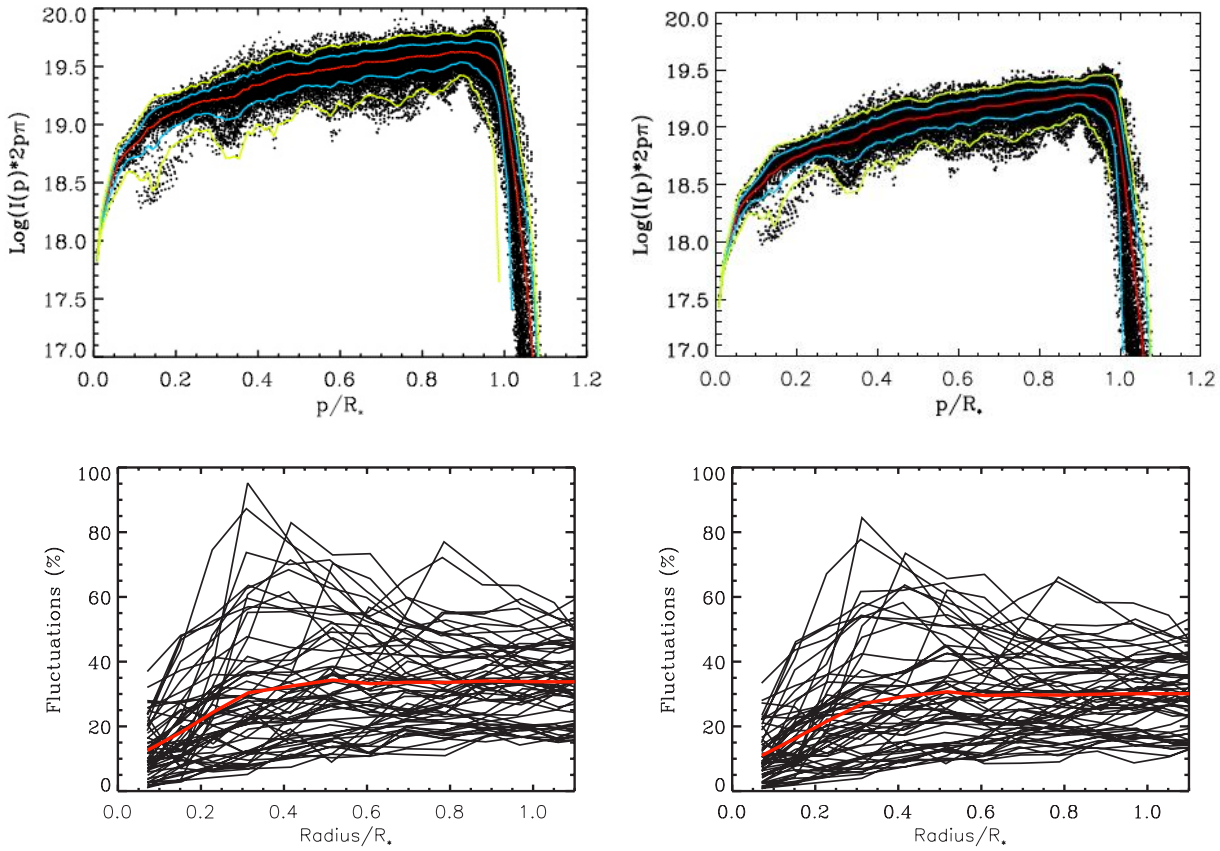

Figure 8.6: *Top left panel:* intensity emerging along the ray with impact parameter p as a function of the impact parameter in the IONIC filter for the snapshot in Fig. 8.5. The red line is the average profile, the blue is the one sigma fluctuation and the yellow line the two sigma fluctuation. *Bottom left panel:* intensity fluctuations at one sigma as a function of the radius for different snapshots of the simulation (3.5 years covered). The radius of the star ($R_\star$), defined as in Sect. 4.2, is equal to 842 $R_\odot$. The red line has the same meaning as in the top left panel. *Top right panel:* intensity emerging along the ray with impact parameter p as a function of the impact parameter in the K222 filter for the snapshot in Fig. 8.5 filter. *Bottom right panel:* intensity fluctuations at one sigma as a function of the radius for different snapshots of the simulation.

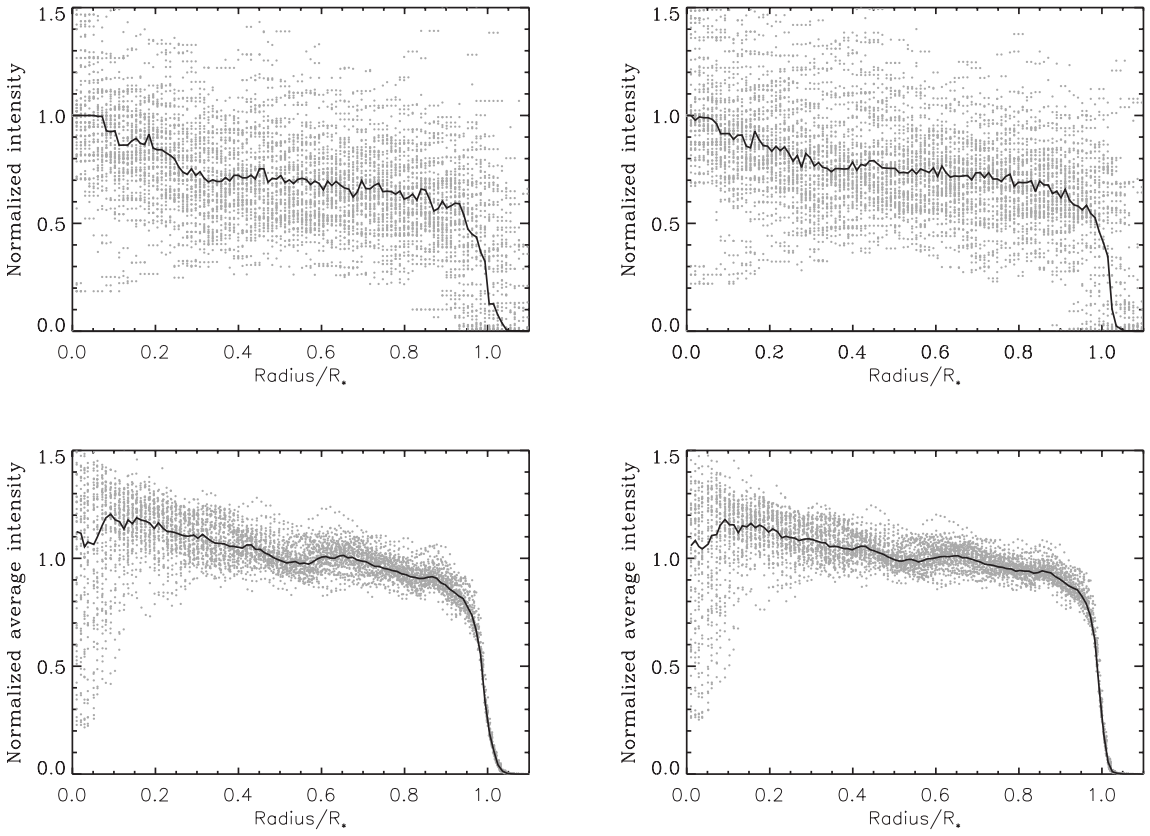

Figure 8.7: *Top row:* scatter-plots of the angular intensity profiles normalized to the intensity at the center of the disk in the IONIC (left) and FLUOR-K222 (right) filters. The solid black line is the median. The snapshot used is the same as in Fig. 8.5. *Bottom row:* scatter-plots of the radially average intensity profiles computed for the IONIC filter (left) and FLUOR-K222 filter (right). The solid black line is the median. There are 57 snapshots with a time-step of ∼23 days (3.5 year covered), $R_\star$ varies from ∼844 $R_\odot$ at 21.5 years to ∼831 $R_\odot$ at 25 years. The intensity profiles are normalized to the subtended area.

8.3.2 The non linear LD law by Claret with new coefficients

The most commonly adopted limb darkening (LD) laws are linear, quadratic, square-root and logarithmic. All these laws are not suitable to fit the complicated intensity profiles of cool supergiants because of their extended wings or sharp edges (Fig. 8.7). Claret (2000) proposed a non-linear law that has been used to compute the LD law in different filters depending on effective temperature, gravities, metallicity and micro-turbulence using the intensity profiles generated by the plan parallel hydrostatic models obtained with the ATLAS-9 code (Kurucz 1992).

My purpose is to re-determine the LD coefficients in the H and K band using this non-linear law for fitting the average intensity profiles computed from the RHD simulations, always keeping in mind that angular and temporal fluctuations of the intensity are really strong for the IONIC-H band filter and for the K222-K band continuum filter. The splitting ratio of the couplers (see Tab. 8.1) are well balanced in the center of the band and poorly in the balanced at the edges, the interferometric sensitivity is always better in the continuum bands compared to the molecular bands. Thus, I choose to use the filter K222 because it samples, with K215, the maximum transmission region in the K band. The law can be written as

$$\frac{I\,(\mathrm{r})}{I\,(0)} = 1 - \sum_{k=1}^{4} \mathrm{a_k} \left(1 - \left(\sqrt{1 - \left(\frac{\mathrm{r}}{\mathrm{R}_\star} \right)^2} \right)^{\frac{\mathrm{k}}{2}} \right) \tag{8.4}$$

where I(r) is the intensity as a function of the radius, r, I(0) is the intensity at the stellar center, $\mathrm{a_k}$ are the LD coefficients and $\mathrm{R}_\star$ is the radius of the star defined as in Sect. 4.2. The law is usually written as a function of μ ($\mu = cos\theta$, and θ is the angle between the line of sight and the radial direction). In my case, I transformed the law using $\mu = \sqrt{1 - \left(\frac{\mathrm{r}}{\mathrm{R}_\star}\right)^2}$ to have the intensity as a function of the radius.
It must be noted that when r=$\mathrm{R}_\star$, $\mu = 0$ and we are at the limb of the star. However, there is also intensity emerging from the region where r>$\mathrm{R}_\star$, that has a minor contribution to the total flux of the star (Fig. 8.6, top panels). Since I want to try to fit the entire intensity profile (from 0<radius/$\mathrm{R}_\star$<1.05), I have also tested a second LD law which can go above the limit of the law by Claret. This second law (a modification of the law found in Ludwig & Beckers 2008) can be written as

$$\frac{I\,(\mathrm{r})}{I\,(0)} = \left(1 - \mathrm{a_1} \left(\frac{\mathrm{r}}{\mathrm{R}_\star} \right)^2 \right) - \left(\mathrm{a_2} \left(\frac{\mathrm{r}}{\mathrm{R}_\star} \right)^4 \right) \cdot \tanh \left[\mathrm{a_3} \left(\frac{\mathrm{r}}{\mathrm{R}_\star} - \mathrm{a_4} \right) \right] \tag{8.5}$$

and in this case $\mathrm{r/R}_\star \lesssim 1.05$. Basically, the two laws have the same number of LD coefficients to fit but Eq. 8.5 has the hyperbolic tangent term that is necessary to reproduce the changing of the slope at about $\mathrm{r/R}_\star \sim 1$ and to fit the stellar limb.
Thus, I have tested these two laws on the same average intensity profile computed in the H band (IONIC filter) from one snapshot of the RHD simulation (Fig. 8.8, left panel) and I have compared them to the LD coefficients derived by Claret (2000) with an ATLAS

model at 3500K, surface gravity = 0.0, solar metallicity and no micro-turbulent velocity (green). The LD from Eq. 8.4 is represented in cyan and the LD from Eq. 8.5 in red. Only the LD from Eq. 8.5 covers the whole intensity profile including the small contribution at the stellar limb (radius/$R_\star$ > 1.0). The LD law by Claret covers the range between 0 < radius/$R_\star$< 1.0. The red curve seems to be closer to the intensity profile at 0.6 radius/$R_\star$, but the cyan one is much closer at 0.5 and 0.90 radius/$R_\star$. In addition, at 0.90 radius/$R_\star$ the law by Claret seems to reproduce well the intensity profile while the LD from Eq. 8.5 is farther of $\sim$ 5%. The green curve is also $\sim$ 5% apart at 0.90 radius/$R_\star$, but it is the closest to the intensity at 0.5 radius/$R_\star$.

In order to establish what law is better, I have computed the visibility curves (Fig. 8.8, right panel) from the radially average intensity profile (solid line), from the LD law from Eq. 8.4 (cyan dashed line), from the LD law from Eq. 8.5 (red dashed line) and from the LD coefficient found for ALTAS model (green dashed line). I found more appropriate to show the visibility curves in the cycles/radius units instead of the usual cycles/arcsec (that I will use in Sect. 8.5 for the direct comparison to the observations). The reverse of the frequency gives the size of the surface structures that affect the visibility curves at this frequency.
The visibility computed from the LD law by Claret with new coefficients seems to be closer to the visibility computed from the intensity average profile especially in the 2nd and 4th lobe (7 and 16 cycle/$R_\star$). Note the improvement with respect to the LD law by Claret with old coefficients from ATLAS model in the 2nd lobe. In the 3rd lobe (12 cycles/$R_\star$, surface structure of about 8% of the stellar radius) the LD of Eq. 8.5 is the closest one.
The LD law by Claret with new coefficient is an improvement with respect to the ATLAS model. This is clearly visible on the top of the second lobe where the LD law by Claret is the closest one with respect to the radially average intensity profile. I remind the reader that the top of the second lobe is crucial for the LD and UD interferometric measurements (see Fig. 7.2).
In addition: (i) it is more difficult to obtain a good fit of the radially average intensity profile with the LD of Eq. 8.5 because the "guess" parameters for the fit must be manipulated intensively; (ii) the LD by Claret has already been published and it is well known and used, new coefficients obtained with this law will be easily introduced for the LD analysis.
Therefore, in the following, I will calculate the limb darkening fit of the intensity average profiles using only the LD law by Claret (Eq. 8.4). Using this law, I neglect the small contribution at radius/$R_\star$>1.0 but I cover the range 0.3<radius/$R_\star$<1.0 that contribute mostly to the stellar flux.

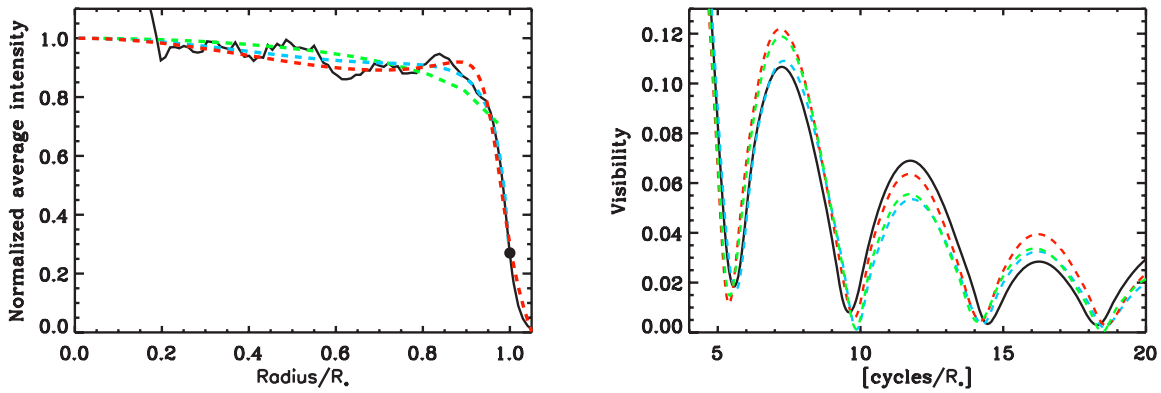

Figure 8.8: *Left panel:* limb darkening fit of the average intensity profile (solid black line) using the LD law by Claret (Eq. 8.4, cyan dashed line) with new coefficients (the black dot shows its limit), the LD law from Eq. 8.5 (red dashed line), and LD by Claret with old coefficients obtained from an ATLAS model at 3500K, surface gravity = 0.0, solar metallicity and no micro-turbulent velocity (green dashed line). The average intensity profile is normalized to 150000 erg/s/cm^2/Å. *Right panel:* Visibility curves computed for one projected baseline from the intensity radially average (black solid line) profile shown in left panel, the other colors have the same meaning as in left panel.

8.3.3 Average LD coefficients in the H and K band (IONIC and K222-FLUOR filters) and temporal variations of the LD profile

In this section, I report the LD coefficients obtained using the LD law by Claret (2000), Eq. 8.4. Fig. 8.7 displays the temporal fluctuations of the radially average intensity profiles and I said that I have to take this into account for the LD fits.
The impact of the temporal evolution is reported in Fig. 8.9 for the H (left column) and K (right column) band. The interval covered is 3.5 years. The maximum and minimum amplitude of the variations (bottom row) strongly increase approaching the stellar limb (radius/R$_\star \sim 1$), while they don't vary too much in the region 0.3<radius/R$_\star$<1.0 (7-8% for the H band and $\sim 5\%$ in the K band). In both cases, these fluctuations are smaller than the angular fluctuations of the intensity profiles.
This means that RHD simulations have an irregular surface pattern due to the convection movements, and this pattern changes with respect to the time. However, the temporal alterations are less strong than the surface inhomogeneities itself. In Sect. 8.4.3, I found that surface inhomogeneities that contribute to the angular dispersion are $\lesssim$25 R$_\odot$.

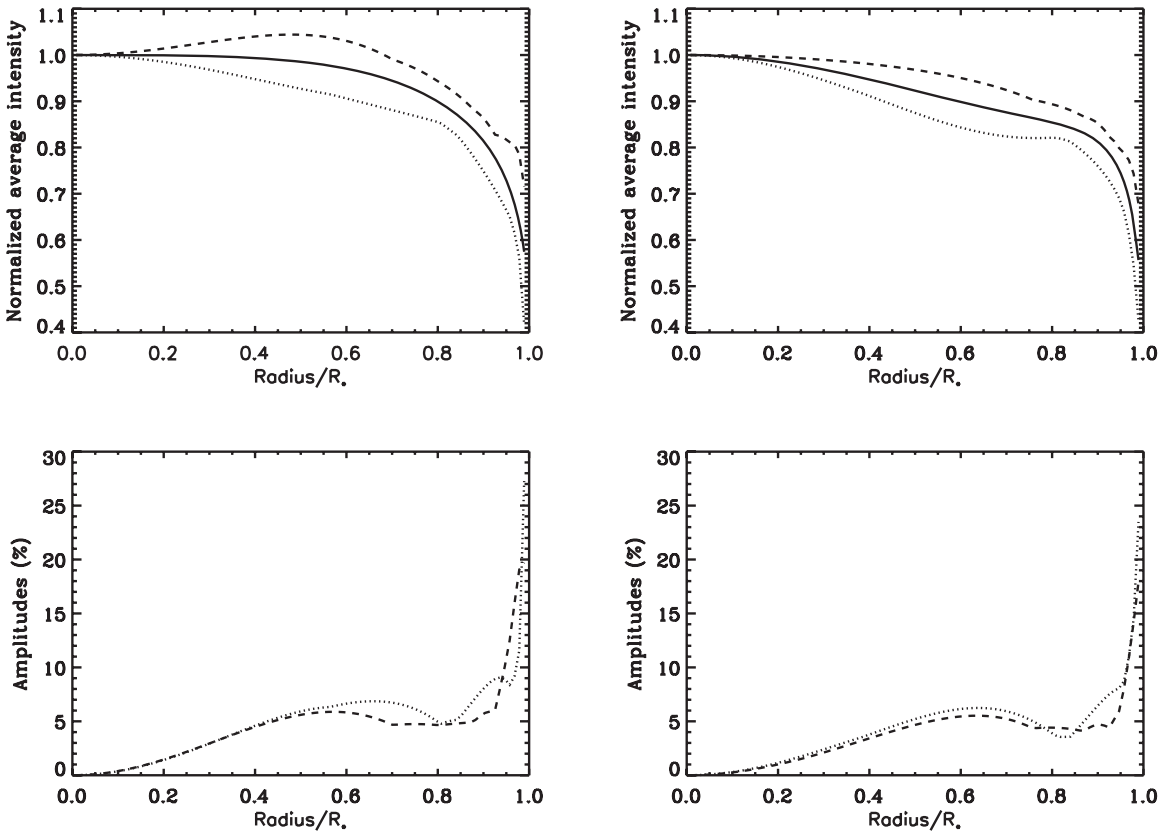

Figure 8.9: *Top row:* temporal and radial average LD profile (solid line) for the H (IONIC filter, left) and K (K222 filter, right) band. Maximum (dashed line) and minimum (dotted line) amplitude variations are also reported. The interval covered is 3.5 years. The profile in the H band are normalized to 150000 erg/s/cm^2/Å, while in the K band to 70000 erg/s/cm^2/Å. *Bottom row:* Amplitude of maximum and minimum excursions with respect to the LD profile in the H (left) and K (right) band. The lines have the same meaning as in top row.

Tab. 8.2 displays the LD coefficients in H band (IONIC filter) and K band (K222 continuum filter) for the angular and temporal average intensity profile. The Table reports also the fluctuations of the coefficients at one sigma with respect to the temporal average (σ_t) and with respect to the angular average (σ_a). The coefficient fluctuations are so big because the intensity profiles fluctuate strongly, as reported above. The surface changes with respect to time are smaller than the surface inhomogeneities itself. The average LD coefficients determined in this work take in consideration the intensity distribution resulting from RHD simulation. The determination of the stellar diameters of RSGs with UD model should account for the correction to the diameter $\theta_{\rm LD}$ including the angular and temporal fluctuations as a source of uncertainty.

Table 8.2: Limb-darkening coefficients for the model described in the text. The LD coefficients correspond to the radial and temporal average profile. σ_t (in %) are the fluctuations at one sigma with respect to the temporal average and σ_a (in %) the fluctuations at one sigma with respect to the angular average.

Wavelenght (μm)	a_1	σ_t (%)	σ_a (%)	a_2	σ_t (%)	σ_a (%)	a_3	σ_t (%)	σ_a (%)	a_4	σ_t (%)	σ_a (%)
1.64 [a]	36.5	78	300	-79.3	80	300	76.6	80	300	-27.3	78	300
2.22 [b]	34.7	67	300	-74.3	70	300	70.8	70	300	24.9	70	300

[a]central wavelength of the corresponding IOTA/IONIC filter
[b]central wavelength of the corresponding IOTA/FLUOR filter

8.4 Visibility Curves and phases

The convection in Red supergiant is characterized by a peculiar convective pattern which has a significant signature on the visibility curves. I seek constraints on these atmospheric motions analyzing the resulting visibility curves and phases.

8.4.1 How the numerical resolution affects the intensity maps

Before starting showing the visibility curves, I want to point out how the numerical resolution of the RHD simulations affects the intensity maps. Fig. 8.10 shows two models with 127^3 (st35gm04n30 in Tab. 4.1) and 235^3 (st35gm04n29) grid points. These simulations have been created from the same starting model (same basic input). Increasing the numerical resolution, small scale structures appear within the large scale granules in 235^3 grid points simulation.

The resolution of the model used in this work is 235^3 grid points model. More in detail, Fig. 8.11 (top panel) shows that small bright artificial patches, a by few pixels wide, are visible all over the map. They do not derive from the radiation transfer computation in OPTIM3D because they are already visible in the bolometric map by Freytag et al.. Therefore, they are a consequence of the low resolution of the RHD models. There are not enough grid points to resolve the narrow temperature jump just below (or around) $\tau = 1$: if convection shifts the atmosphere by half a grid point upwards the stratification changes somewhat and the emergent intensity changes too, even if the column is somewhere in the middle of a granule where all columns should give essentially the same intensity. Tests on the source function and opacity interpolation have been carried out inside CO^{5}BOLD causing instabilities of the code (Freytag private communication). The unique solution is to increase the number of grid points, and that implies bigger and faster computers (see Sect. 2.3.4).

The bottom panel of Fig. 8.11 shows how the visibility curves are affected by this artificial structures. The black curve is the visibility curve computed for one projected baseline and the red one is computed after applying a median smoothing that replaces each point with the median of the neighborhood with a width of 3x3. The largest differ-

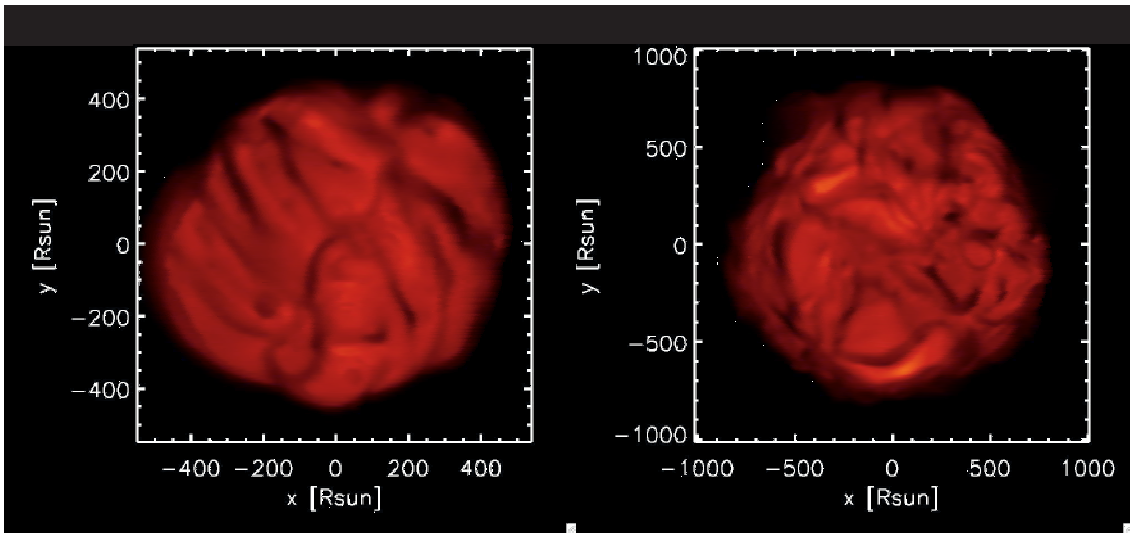

Figure 8.10: Maps of the linear intensity computed in the H band IONIC filter (Fig. 8.4, bottom panel) for the two models described in the text: left 127^3, and right 235^3 grid points. The snapshots are different and the models have been created form the same starting model (see text). The range of the intensity is [0,300000] erg/s/cm^2/Å.

ences are noticeable at 0.035 cycles/$R_\odot$ (corresponding to surface structures less than 28 $R_\odot$, i.e., ∼3.3 pixels).
In the following sections, I will always apply the median smoothing to compute the visibilities in order to avoid pollution by artificial structure. I can do this without changing the final result and the comparison to the observations because the visibility curves differ only at the 7th lobe and today interferometers are not able to obtain valuable data at this high frequencies. In addition, I will analyze the visibility curves up to the 4th lobe (∼50 $R_\odot$) which is still far from these frequencies that are closer to the simulation numerical resolution limit (1 grid point corresponds to about 8.5 $R_\odot$).

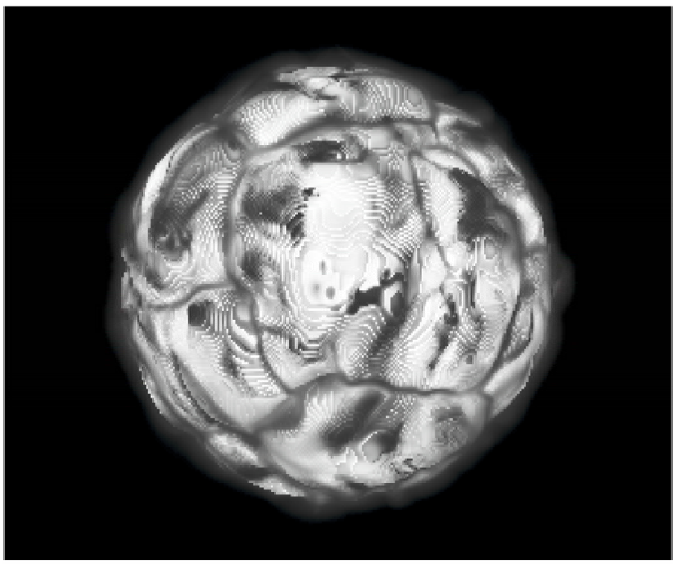

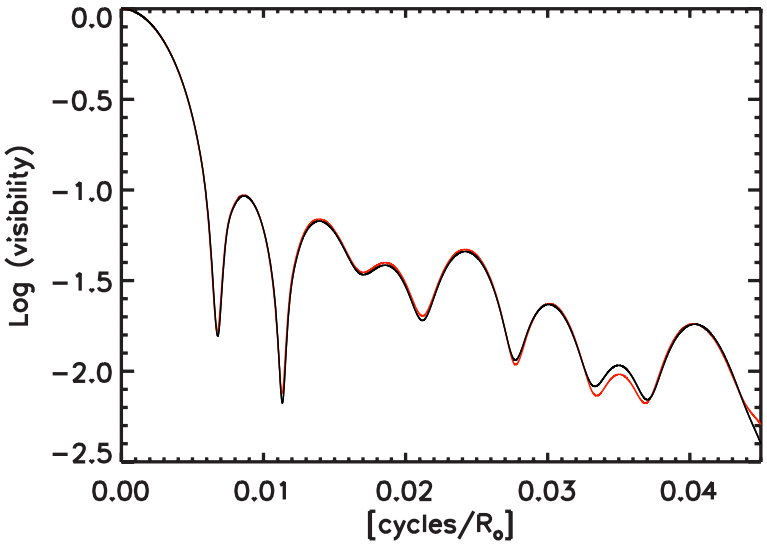

Figure 8.11: Numerical resolution impact on the intensity maps. *Top panel:* Intensity map of one snapshot computed in the H band IONIC filter (Fig. 8.4, bottom panel) represented using the histogram equalization algorithm in order to underline the artificial pixel structures on the stellar surface. *Bottom panel:* Visibility curves compute as a function of cycles/$R_\odot$ for the unchanged intensity map (black curve) and for the same map after applying a median smoothing that replaces each point with the median of the 3x3 neighborhood (red curve).

8.4.2 The first lobe

Usually, in interferometry, the visibility is in a direct relation with the stellar properties (angular radius, LD coefficients, see Eq. 7.17) and it could be used in a least- squares procedure to obtain the stellar radius and LD coefficients from interferometric measurements. This is done using uniform disk (UD) or limb darkened-disk models. In addition, the interferometric measurements normally cannot distinguish between limb-darkened disk and UD unless the data are taken beyond the first null of the visibility function.
The determination of the stellar diameters is thus done in two steps: first the diameter $\theta_{\rm UD}$ of the uniform disk model (Eq. 7.18) is fitted to the visibility data, and then $\theta_{\rm UD}$ is multiplied with a correction factor derived from model atmospheres to obtain the diameter $\theta_{\rm LD}$. The latter is used to find the effective temperature

$$T_{\rm eff} = \left(\frac{L}{4\pi\sigma R^2}\right)^{1/4} = \left(\frac{4f_{\rm bol}}{\sigma\theta_{\rm LD}^2}\right)^{1/4} \tag{8.6}$$

where L is the luminosity of the star, R the stellar radius, σ is the Stefan-Boltzmann constant and $f_{\rm bol}$ the bolometric flux.

RSG (and cool stars in general) have not an uniform brightness distribution and they have surface structures that strongly affect the visibility curves and consequentially make the uniform disk or limb-darkened hypothesis inadequate.

I found that the visibility curves behavior can be separated into two different groups: the first lobe (i.e., from 0 cycles/$R_\odot$ to the first zero point) and the second, third, fourth lobe. In this section, I start analyzing the first lobe.
Fig. 8.12 shows the visibility curves computed from the intensity map of one snapshot (Top row in Fig. 8.14) of the best simulation (st35gm03n07 in Tab. 4.1) collected for 36 different angles (grey curves) in the IONIC filter (left panel) and K222-continuum filter (right panel). The red dashed line is a uniform disk of 16 mas and the solid black line is the average limb darkening profile of the model (see Tab. 8.2).
A dispersion of the visibility curves (grey) around the LD profile and UD profile is noticeable in Fig. 8.12. The visibility between 0.003 and 0.005 cycles/$R_\odot$ correspond to the large and persistent granules ($\sim$250 to $\sim$500 $R_\odot$). This signature is really strong in all the visibility curves both in the H and K bands.

The dispersion due to the convection-related surface structures must be also considered. For this purpose, I examine the fluctuations at one sigma of the visibility curves with respect to the average value in two ways:

- the *temporal evolution*, fixing one angle and following time-step by time-step of the RHD simulation for 3.5 years with a step of $\sim$23 days.
- the *spatial evolution*, considering a single snapshot and computing the visibilities for 36 different angles with a step of 5°.

Fig. 8.13 shows the temporal fluctuations of the visibilities for four fixed angles (black lines) and the angular fluctuations for five snapshots (red lines) in the H band (IONIC

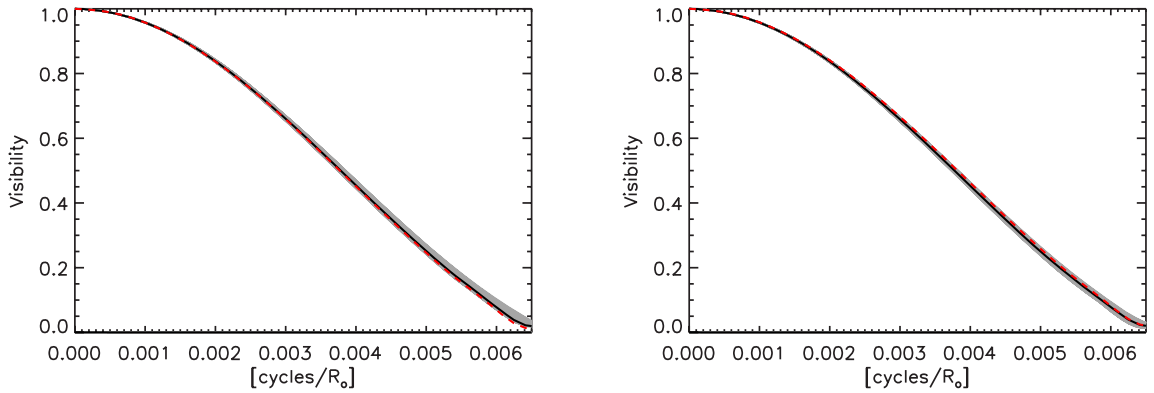

Figure 8.12: The first lobe: the visibility curve computed from the LD profile derived from Tab. 8.2 (solid black line) is superposed to the synthetic visibilities (grey) in the IONIC filter (left panel) and K222 filter (right panel) The grey curves correspond to 36 different angles with a step of 5° for the snapshot in Fig. 8.14. The red dashed curve is a uniform disk model.

filter). The visibility fluctuations are lower than 1% at ∼0.0028 cycles/$R_\odot$ (at this frequency, the visibility is greater than 70%). In the first lobe, there is not a clear distinction between temporal and spatial fluctuations.The fluctuations are ∼ 5% at 0.005 $R_\odot^{-1}$ and close to ∼ 10% at 0.006 $R_\odot^{-1}$. Thus, the measure of the stellar diameter with UD and LD models should take into account this dispersion as an additional uncertainty.

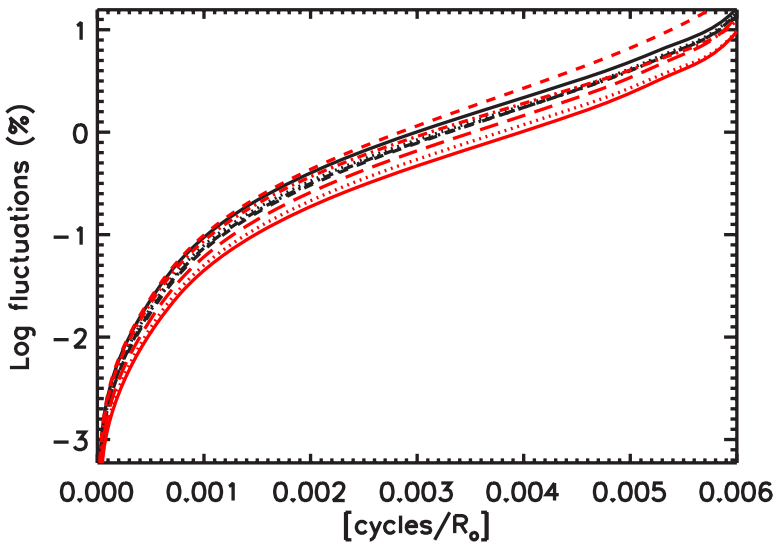

Figure 8.13: Fluctuations (1 sigma) of the visibility curves as a function of frequency in the first lobe. Black curves indicates temporal fluctuations for fixed angles (the time covered is 3.5 years), while red curves correspond to the spatial fluctuations for different snapshots ∼230 days apart.

8.4.3 The second, third, and fourth lobe: signature of the convection

Fig. 8.14 shows an enlargement of the visibility curves focused on the second, third and fourth lobes. The visibilities (grey curves, bottom row) have been computed as in previous section (36 angles in the IONIC, right panel, and K222, left panel, filters) from the RHD snapshot reported in top row. In addition to the LD visibility curve derived from Tab. 8.2 (black solid line) and UD visibility curve of 16 mas (dashed line), the Figure displays also 4 different visibility curves derived for 4 particular angles over-plotted on the intensity maps (top left panel).

If I choose, for example, the angle 135° (green line) in the H band (top left panel in Fig. 8.14), the projected baseline crosses one big dark spot of about 150 $R_\odot$ (at x=-150 $R_\odot$, y=150 $R_\odot$) and a second one of few $R_\odot$ (at x=-500 $R_\odot$, y=400 $R_\odot$). The same angle in the K band (top right panel) crosses the same regions. These small scale (compared to the big, 400-500 $R_\odot$, granule) structures affect the visibility curves that deviate from the UD disk visibility and appear different in the H or K band. The green visibility curve derived from the H band image is higher in the third lobe (corresponding to surface structure of ~ 70 $R_\odot$) than the one computed from the K band image; in both case, the fourth/fifth lobe ($\sim 0.020 - 0.025$ cycles/$R_\odot$) shows an increase of the visibility signal that derives from the structures of $\sim 40 - 50$ $R_\odot$.

The characteristic size distribution on the stellar surface can be derived from the visibility curves: the contribution of small scale convection-related surface structures increases with spatial frequencies. In the second lobe, we have the contribution of structures of ∼120 $R_\odot$ (15% of the stellar radius), in the third lobe of ∼70 $R_\odot$ (8% of the stellar radius), and in the fourth lobe of ∼50 $R_\odot$ (6% of the stellar radius). The RHD simulation's limits due to the numerical resolution is about 0.04 cycles/$R_\odot$ (∼25 $R_\odot$, 3% of the stellar radius) because each grid point of the model corresponds to 8.6 $R_\odot$ and 2 or 3 grid points (25.8 $R_\odot$) would coincide to the limit found in Sect. 8.4.1.
The prediction of the RHD simulation can be confirmed by interferometric observation distributed at different frequencies in order to characterize the typical size of the convection pattern.

As in Sect. 8.4.2, I analyze the spatial and temporal fluctuations at one sigma with respect to the average value in the H band (IONIC filter). Fig. 8.15 shows the temporal fluctuations of the visibilities for four fixed angles (black lines) and the spatial fluctuations for five snapshots (red lines).
As for the first lobe, there is not a clear distinction between spatial and temporal fluctuations. In addition, the fluctuations clearly increase with spatial frequencies.
The different peaks in the Figure correspond to the zero points and they have almost the same fluctuation ($\sim$ 35%) over the whole frequency; however, the position of the zero points fluctuate also and sometimes there is a double peak. The "valleys" at 0.009, 0.014 and ∼0.020 cycle/$R_\odot$ correspond to the top of the second, third and fourth lobe.
The fact that there is not a clear distinction between the different fluctuations is surpris-

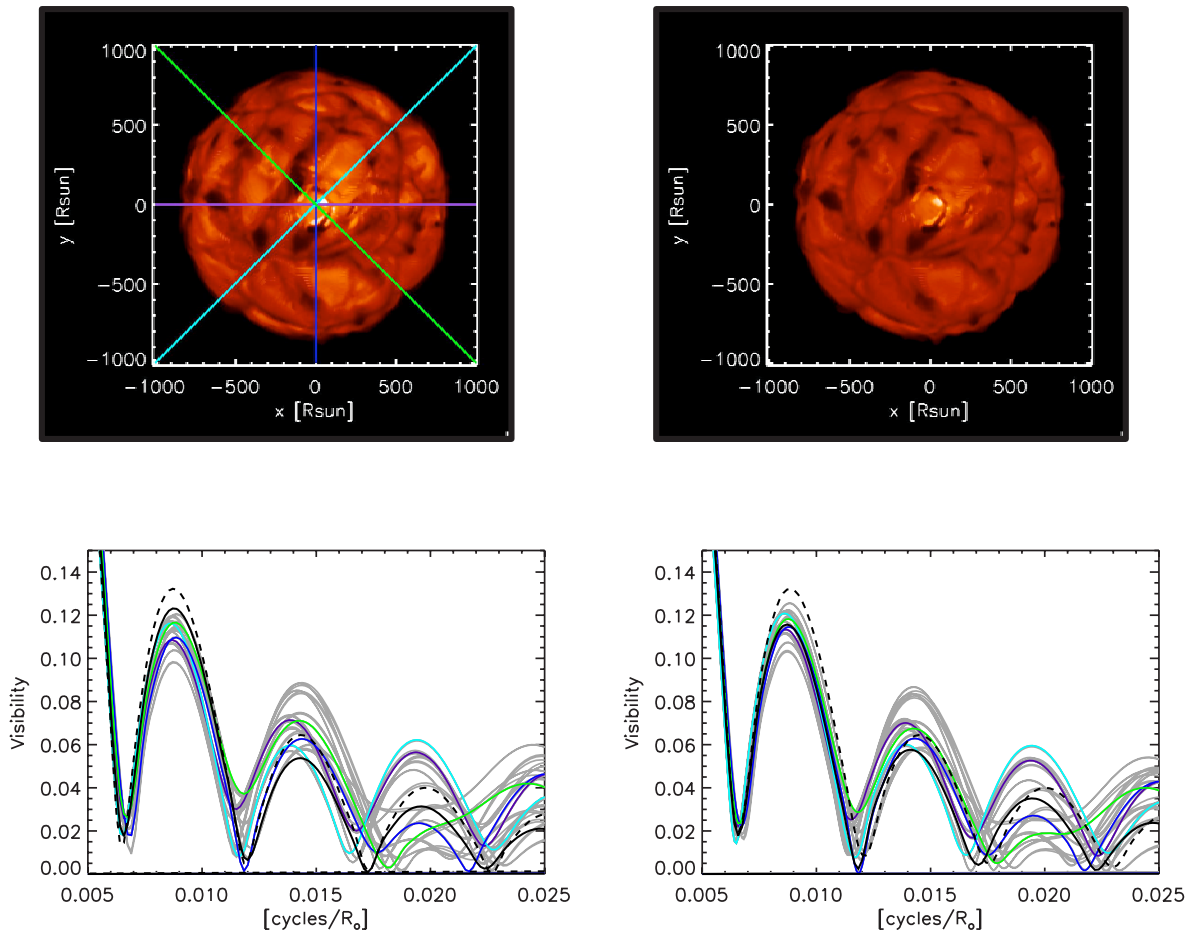

Figure 8.14: *Top panels:* intensity maps in the IONIC (left panel, a scale is used within the range [0,310000] erg/s/cm^2/Å) and K222 (right panel, [0,150000] erg/s/cm^2/Å) filters. The colored lines delineate four angles corresponding to the colored visibility curves in lower panels. *Bottom panels:* the visibility curve computed from the LD profile derived from Tab. 8.2 (solid black line) is superposed to the synthetic visibilities (grey and colors) in the IONIC filter (left panel) and K222 filter (right panel). The grey curves correspond to 36 different angles with a step of 5° for one snapshot. The dashed curve is a uniform disk.

ingly because in Sect. 8.3.3 I found that the angular (or spatial) intensity fluctuations are stronger than the temporal ones. Thus, I have checked that the visibility spatial fluctuations become systematically larger than the temporal ones only from frequency 0.035 $R_\odot^{-1}$ (i.e., the numerical resolution limit, Sect. 8.4.1). Therefore, I can say that surface structures of $\lesssim$25 $R_\odot$ contributes to the intensity angular dispersion seen in Sect. 8.3.3.

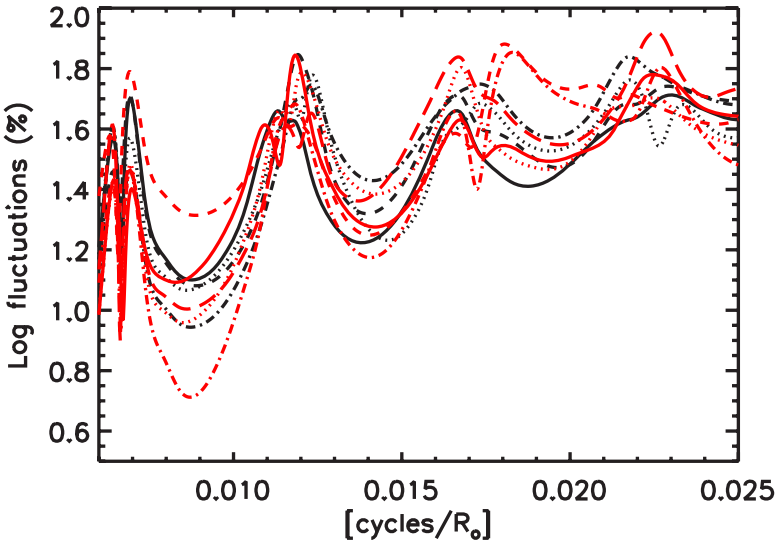

Figure 8.15: Second, third and fourth lobe fluctuations (1 sigma) of the visibility curves as a function of spatial frequencies. Black curves indicates temporal fluctuations for fixed angles, while red curves correspond to the spatial fluctuations for different snapshots. There is not a clear distinction between temporal and spatial fluctuations.

The conclusion is that synthetic visibilities derived from RHD models show clear deviations from the circular symmetry and have stronger fluctuations. This is particularly remarkable in the second, third and fourth lobes and higher.

There are two ways to detect the signature of the convection in the visibility curves:

- looking for the angular visibility fluctuations observing with the same telescope configuration (covering high spatial frequencies) using the Earth rotation in order to span enough values in the UV plane. Typically azimuths of 20 to 100° should be enough.
- looking for the temporal visibility fluctuations observing at two (or more) epochs ∼1 month apart with the same telescope configuration.

The interferometric data so far cover only the first lobe, the first null and the second lobe when possible. In this work, I want to stress that the interesting information is indeed in the second, third and fourth lobe, beyond the simple determination of the stellar radius and limb darkening coefficient.

8.4.4 Impact of the water vapor line on the visibility in IONIC filter

Stellar water vapor lines strongly affect the intensity maps and the visibility curves in the IONIC filter. The red line in Fig. 8.4 (bottom panel) shows that strength of waver vapor lines are lower than the CO and CN bands.

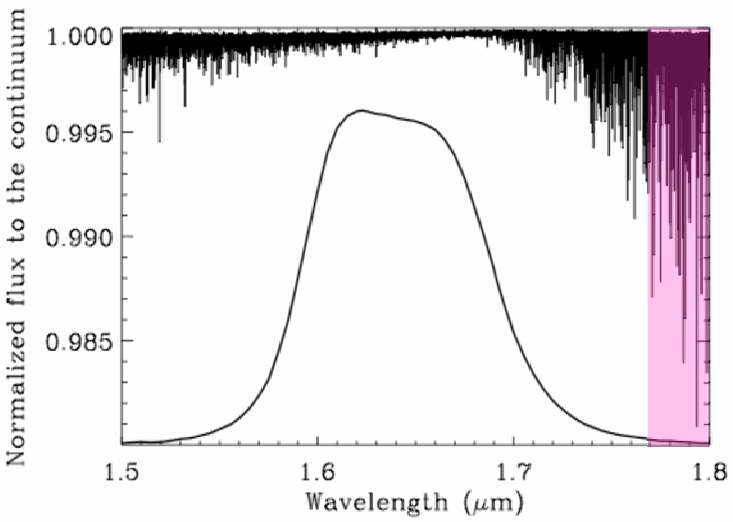

Figure 8.16: The IOTA filter as in Fig. 8.4 (bottom panel) together with the synthetic spectrum of water vapor only. The pink region shows where the telluric lines that disturb the stellar spectra are more present.

Hoverer, Fig. 8.16 displays that the line density is really high in the H band and this clearly affects the intensity maps. Basically, the huge amount of line veils the stellar surface and increases the opacity.

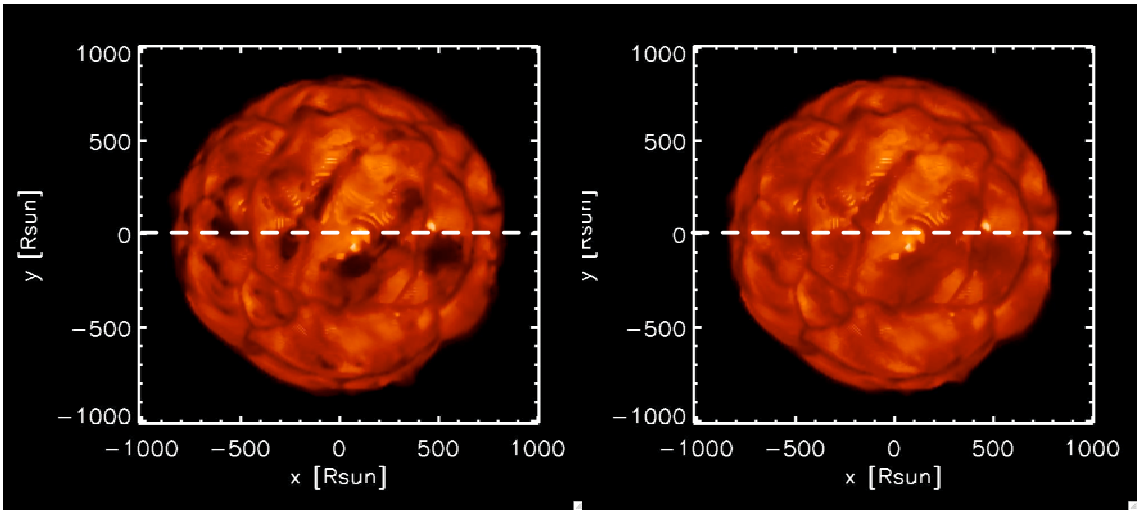

Figure 8.17: Intensity maps in the IOTA filter considering the water vapor lines (left panel) and not considering them (right panel). A scale is used within the range [0,310000] erg/s/cm^2/Å. The dashed white line is the direction of the projected baseline used for computing the visibility curves in Fig. 8.18.

Fig. 8.17 shows the effect on the synthetic maps. The darker region in right panel (no-water vapor lines) becomes darker in left panel (yes-water vapor lines) while the brighter regions remain unchanged. As a consequence the ratio between dark and bright areas increase. Water vapor lines contribute to the line absorption that takes place in the outer layers ($\tau_{\text{continuum}} \lesssim 0.1$) and they veil the continuum intensity coming from the deeper layers ($\tau_{\text{continuum}} \sim 1$).

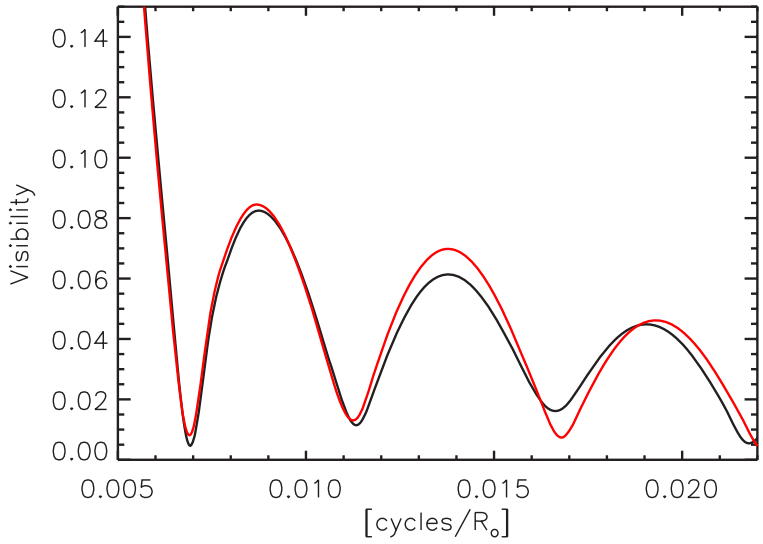

Figure 8.18: Visibility curves computed on the projected baseline (dashed white) in Fig. 8.17. The black line correspond to the no-water vapor lines intensity maps (right panel in Fig. 8.17) and the red one with the water vapor lines included (left panel).

The sharper dark scale structures within the large granules affect strongly the visibility curves, especially at higher frequencies (Fig. 8.18). In the second lobe (0.009 cycle/$R_\odot$) there are no large differences between the black (no-water vapor lines) and red (water vapor lines included) curves. However, at 0.014 cycles/$R_\odot$ (corresponding to surface structures of $\sim$70 $R_\odot$) the visibility of the intensity map with water vapor lines is about 15% higher that the other one, while at 0.020 cycles/$R_\odot$ ($\sim$ 50 $R_\odot$) the signal is again similar but slightly shifted.
Introducing the water vapor lines induces an increase of the visibility signal due to the surface structures of $\lesssim$70 $R_\odot$.

8.4.5 Granulation contrast and its impact on visibilities

The granulation contrast affects the fluctuations of the visibility curves.
In order to find a law that relies these quantities, I have reduced artificially the contrast of one image in IONIC filter obtained with st35gm03n07 simulation (Fig. 8.19, first frame): I define the contrast as the difference between the LD intensity map and the intensity map of the snapshot.
Fig. 8.19 shows that diminishing the contrast, the surface structures tend to disappear

getting closer to the limb darkening intensity distribution (extreme right column). This is noticeable also in the visibilities (Fig. 8.20, right panel), where the curve obtained from the unchanged contrast (black solid line) tends to the LD visibility curves (red line) when decreasing the contrast (dotted and dashed line).

The one sigma fluctuations of the visibility curves with respect to the average value computed from the images in Fig. 8.19 (36 angles with a step of 5°) depend directly on the intensity surface contrast. The highest fluctuations correspond to the highest contrast caused by the surface inhomogeneities. In Fig. 8.20 (left panel), when the contrast is reduced, the surface structures tend to fade and the resulting visibility fluctuations decrease for the second lobe (frequency ∼0.009 $R_{\odot}^{-1}$) and third lobe (frequency ∼0.014 $R_{\odot}^{-1}$). The fluctuations of the fourth lobe (frequency ∼0.02 $R_{\odot}^{-1}$) decrease somewhat less linerarly.

Thus, the visibility fluctuations are proportional to the granulation contrast.

The prediction of the RHD simulation can be used to determine the granulation contrast from the visibility fluctuations: for example, absorption lines show larger fluctuations than the continuum (Fig. 8.22). From these fluctuations, the information about the contrast between different depths in the atmosphere can be retrieved.

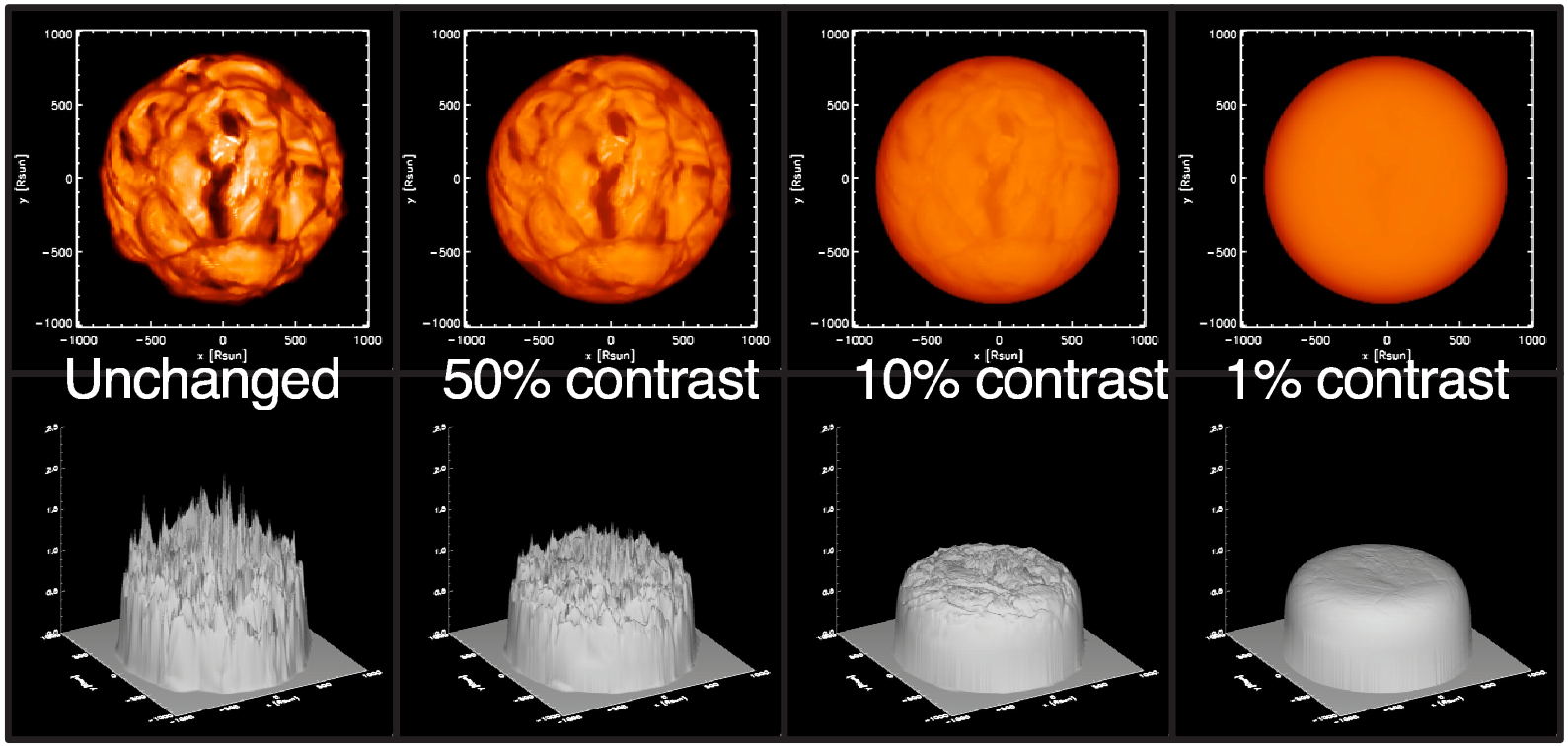

Figure 8.19: Linear intensity maps from one time-step in IONIC filter computed from st35gm03n07 model. *Top row:* the unchanged surface contrast (top left panel) and for the other panels, the per-cent of the contrast left after reduction is indicated. *Bottom row:* three dimensional plot of the intensity.

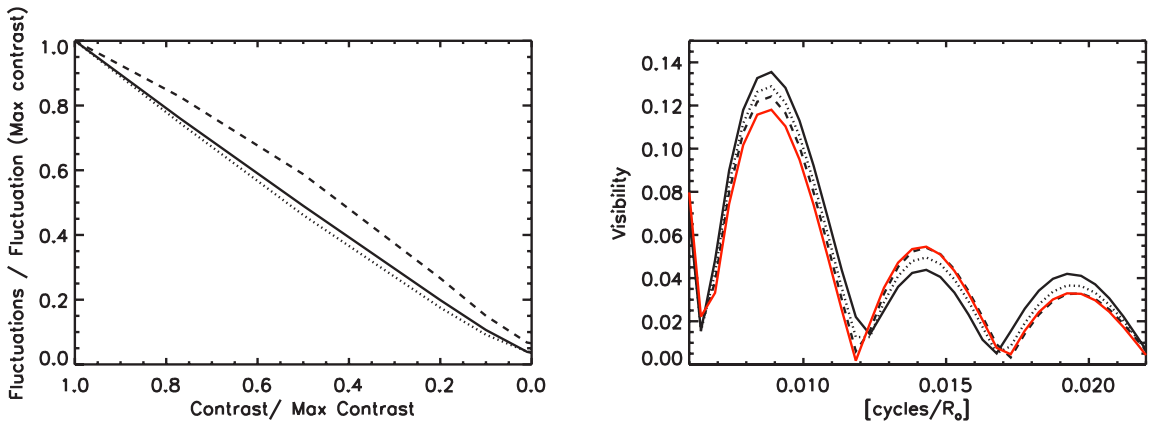

Figure 8.20: *Left panel:* fluctuations (one sigma) of the visibility curves (computed for 36 angles with a step of 5°) at the top of the second lobe (solid line), the top of the third lobe (dotted line) and the top of the fourth lobe (dashed line). The fluctuations and the contrast are normalized to the fluctuations of the maximum contrast and the maximum contrast respectively. *Right panel:* Visibility curves for one angle. The unchanged contrast visibility is the solid line, 50% of the contrast the dotted line, 10% of the contrast the dashed line and the red solid line the LD profile.

8.4.6 Importance of spectral resolution in interferometry

Using a band filter (such as IONIC), the information of the continuum (or of a line) is mixed with the contribution from the features (e.g., CO lines in H band). For example, Chiavassa et al. (2008) and Fig. 8.21 show that in the region around 1.6 μm, wavelengths corresponding to the continuum show large scale granules; while for wavelengths where the CO contributes, small scale structures appear. Observing the surface at different wavelengths, the unit optical depth is encountered in higher layers for wavelengths with high opacities (e.g., absorption lines) and in deeper layers for wavelengths with low opacities (the continuum). Thus, the emerging intensity from the deeper layers (bright hot regions in the Figure) is veiled by the spectral lines that absorb the intensity in the outer layers (dark cooler patches in the Figure).
This affects considerably the visibility curves.

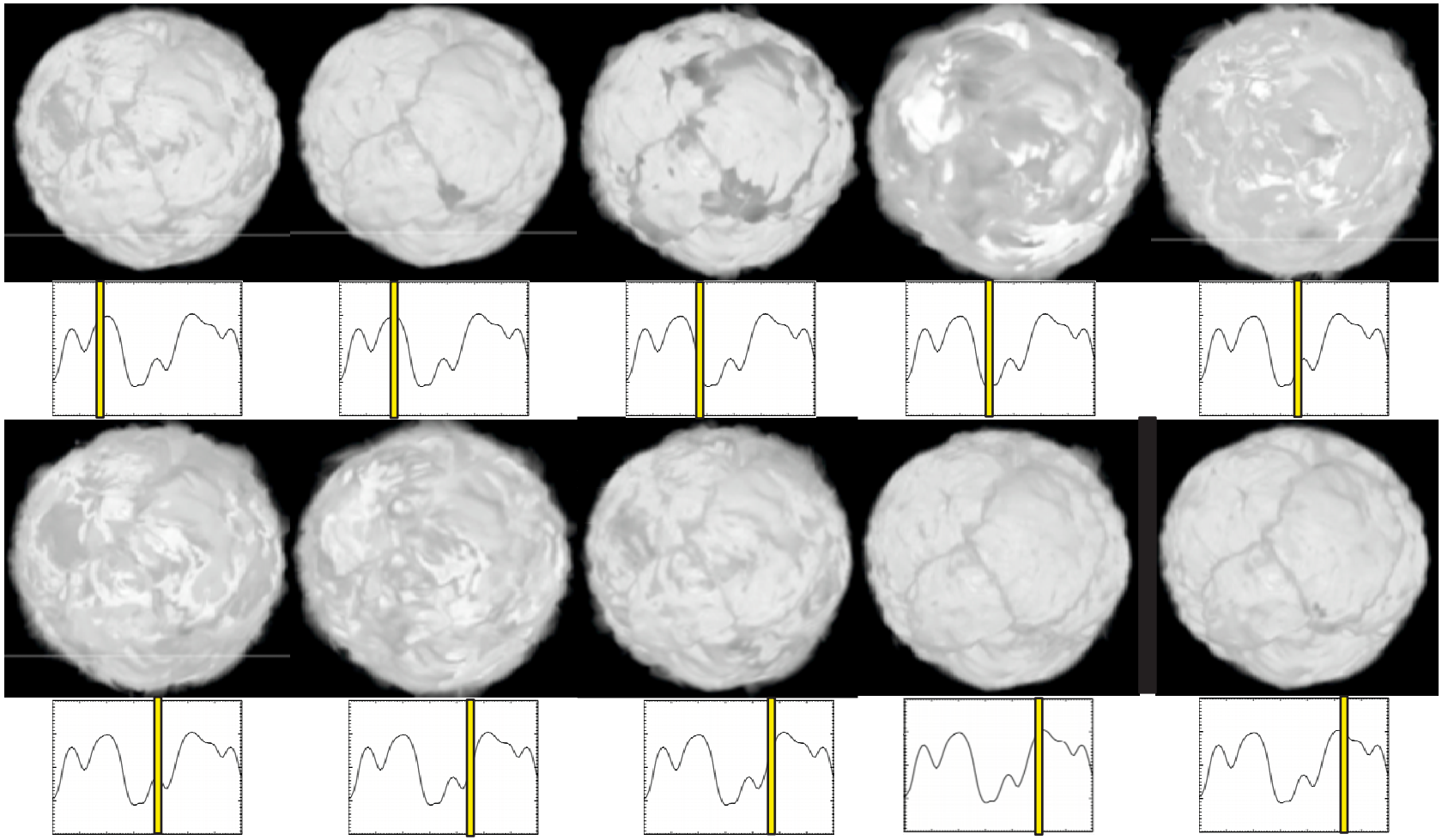

Figure 8.21: Sequence of logarithmic intensity maps (range is [-2,2]) probing different wavelength in the spectrum (yellow line) around the H^- minimum opacity (the spectral range is [1.5885-1.5892] μm ;Chiavassa et al. 2008). The model used for this computation is st35gm03n08 (Tab. 4.1).

At different wavelengths, the visibility curves are completely different. This is reported in Fig. 8.22 for $\sim$ 2.15 μm (the continuum, left column) and $\sim$ 2.3 μm (CO line at $\lambda = 23097.094$ Å, $\log(gf)$=-4.195 and χ=1.476 eV, right column).
A first important point concerns the intensity scale of the two maps (top panels). The CO lines absorb the emerging intensity from deeper layers (the continuum in top left panel) and the map looks darker.
Another difference concerns the visibility fluctuations at one sigma with respect to the average visibility. The first lobe (frequency < 0.0055 $R_{\odot}^{-1}$, i.e., lower than the first zero), the visibility fluctuations of the CO line (dotted line in bottom left panel) are larger than the continuum (solid line), indicating that the radius of the star is bigger in CO bands than in the continuum because of the contribution of the outer layers.
In the second, third and fourth lobe (frequency > 0.0055 $R_{\odot}^{-1}$, bottom right panel), the visibility fluctuations of the CO line are always >10% and in the fourth lobe they are even >30%. This visibility fluctuations could be easily measured but if the surface contrast is 50% smaller, the fluctuations are 50% smaller on the top of the second and third lobe and 40% on the top of the fourth lobe.

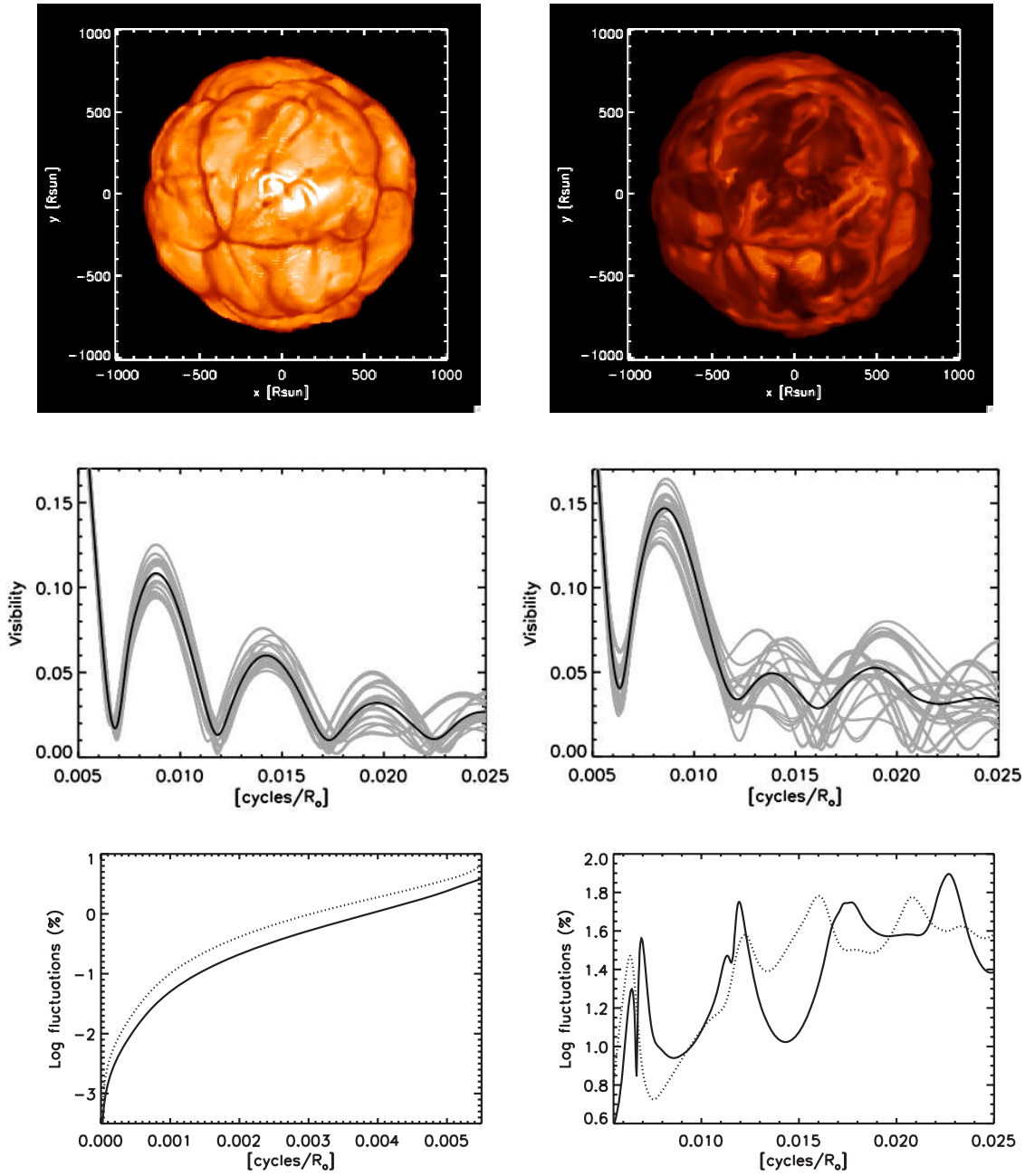

Figure 8.22: Left column shows the 21500±0.1104 Å and right column is 23097±0.1104 Å. *Top row:* Maps of the linear intensity (top frames, a scale is used within the range [0,11000] erg/s/cm^2 Å). *Central row:* visibility curves computed from the intensity map above corresponding to 36 different angles with a step of 5° for one snapshot (grey). The black line is the average profile. *Bottom row:* two enlargements of the logarithm of the fluctuations (one σ) with respect to the average visibility (solid curve for the continuum and dotted curve for the CO line).

Interferometers such as VLTI-AMBER provide a spectral dispersion of R=35, 1500 or 12000. In order to predict how the visibility would behave with respect to the wavelength, I analyzed separately these three spectral resolutions using st35gm03n07 simulation (Tab. 4.1).

For the low spectral resolution (R=35), I computed maps centered on 1.6 μm (H band) and 2.33 μm (K band - CO) for one snapshot of the simulation. The intensity maps are reported in Fig. 8.23 (top row). From them, I have calculated the visibility curves for the three maps and for 18 angles with a step of 10°.

The low AMBER spectral resolution is not enough to characterize the difference between the H and K band. This is noticeable in 8.23 (bottom panels) where there is not an evident difference between the visibility fluctuations derived from the three intensity maps (top panels).

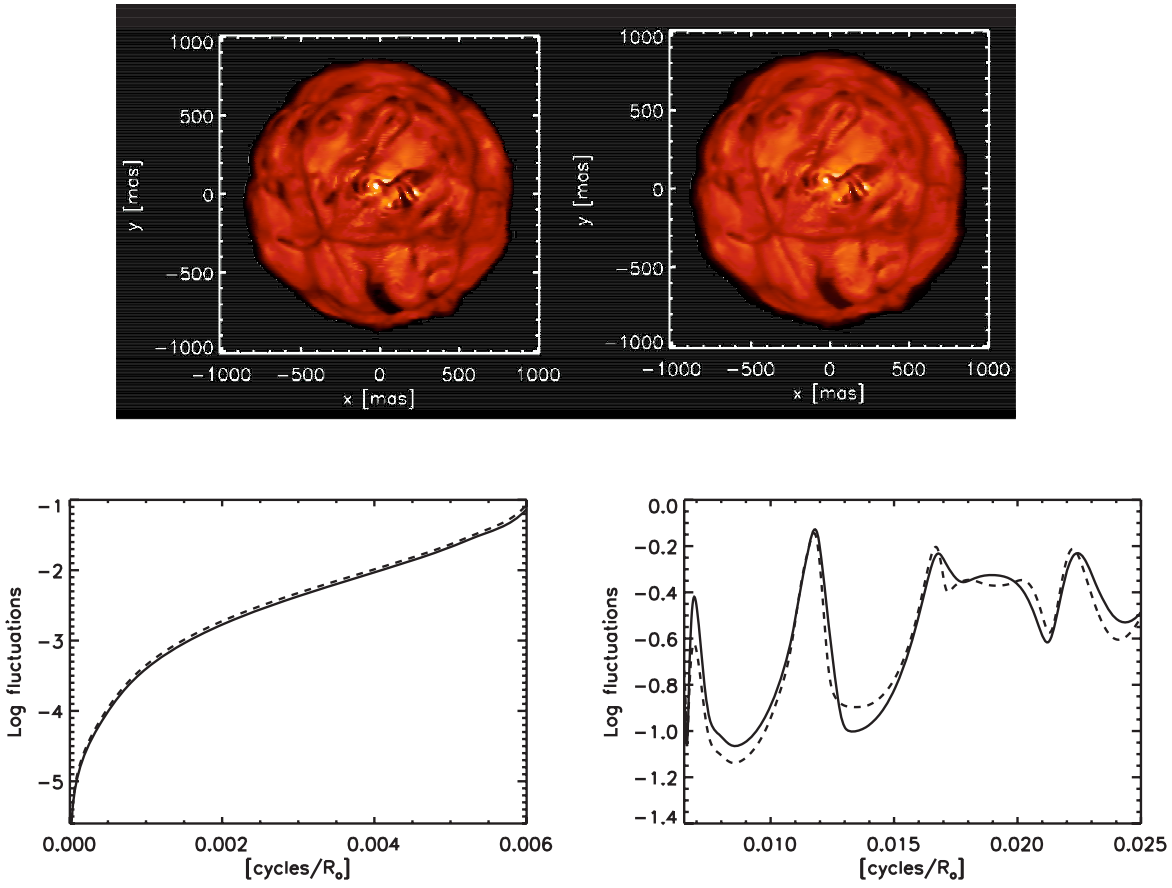

Figure 8.23: *Top row:* Maps of the linear intensity computed at 1.6±0.0228μm (left, a scale is adopted within a range of [0,310000] ers/s/cm^2/Å) and 2.33±0.0333μm (right, [0,90000] ers/s/cm^2/Å). *Bottom panels:* two enlargements of the logarithm of the fluctuations (one σ) with respect to the average visibility. The solid curve corresponds to the H band at 1.6 μm and the dashed line to the K band at 2.33 μm.

For the medium and high resolution (R=1500 or 12000), I computed the wavelength dependent visibility in the H band around 1.6 μm for a snapshot of the simulation. Fig. 8.24 displays a three-dimensional view of the visibility curves with a resolution of 12000 (top left) and 1500 (top right). The simulated star has been scaled to an apparent diameter of 45 mas at a distance of 173.5 pc. Strong fluctuations are already noticeable at the minimum points and on the top of the different lobes.
Considering now the top of the second lobe ($\sim$35 arcsec^{-1}), the bottom panel shows the scatter plot of the visibility curves for this selected frequency, computed for one baseline angle as a function of the wavelength. Small black dots belong to R=12000 while the big red dots to R=1500. The synthetic spectrum binned to a resolution of 12000 is overplotted (thin solid line).
The visibility is clearly dependent on the wavelength. Qualitatively, the visibility dispersion is comparable to the spectral lines. In order to characterize the convective pattern, it is crucial to have high spectral resolution to analyze the variations of the interferometric data between different spectral features and continuum. The H band around 1.6 μm is a good target for observing this wavelength dependance because the dispersion is strong.

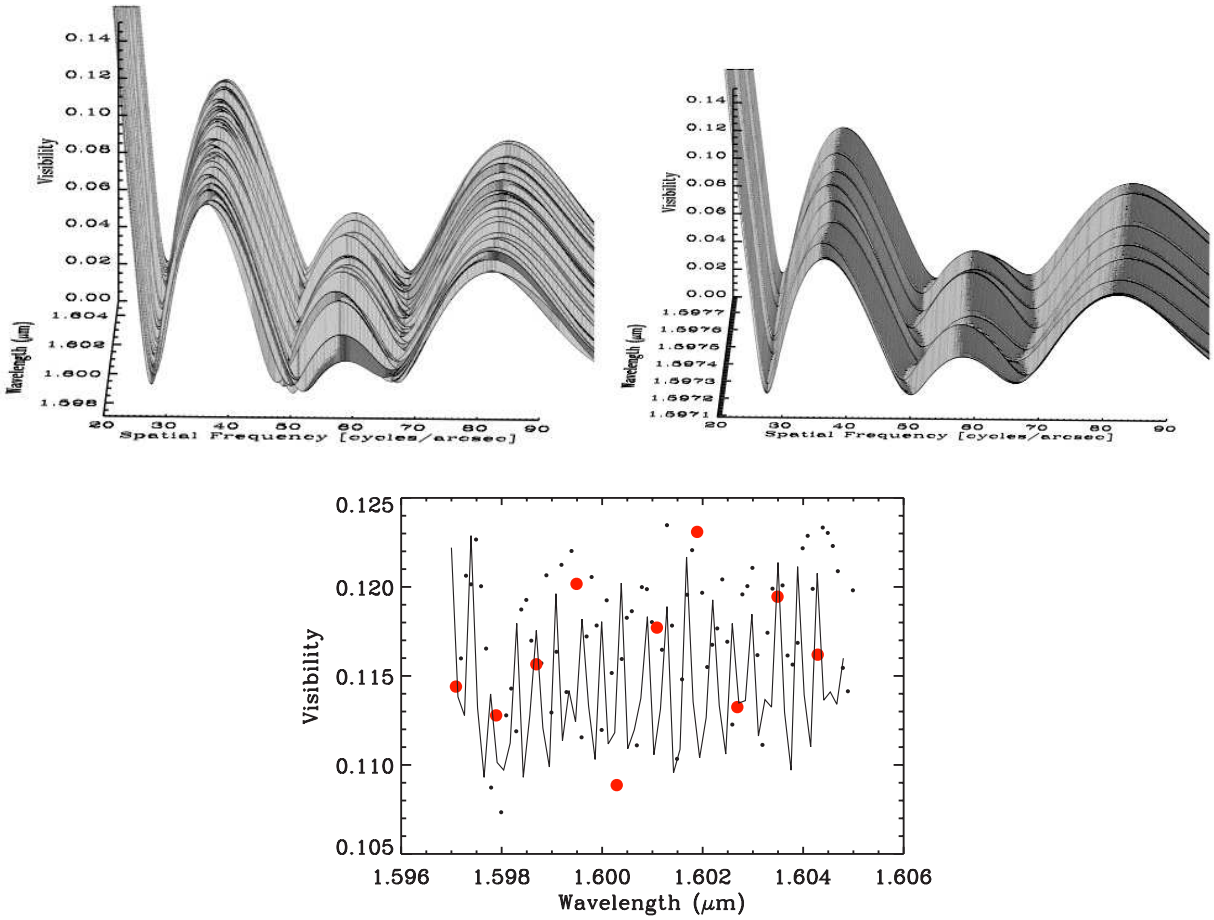

Figure 8.24: *Top left panel:* three-dimensional view of the visibility curves as a function of the wavelength. The spectral resolution is 12000. *Top right panel:* same as in top left panel but with a spectral resolution of 1500. *Bottom panel:* Scatter plot of the visibility as a function of wavelength at one selected frequency (∼35 arcsec^{-1}, ie. the top of the second lobe) computed for one angle. The small black dots correspond to the highest resolution with AMBER (12000), while the big red dots to the medium resolution (1500). The synthetic spectrum binned to a resolution of 12000 is over-plotted (thin solid line).
The stellar parameters of this snapshot are: L = 98419.83 $L_\odot$, R = 836.48 $R_\odot$, T = 3534.04 K and log(g) = -0.34. The simulation has been scaled to an apparent diameter of 45 mas at a distance of 173.5 pc.

8.4.7 Closure phase: departure from circular symmetry

The closure phase gives a complementary information to unveil the asymmetry of the RSGs (see Sect. 7.4). Fig. 8.25 shows the scatter plot of the closure phase of one snapshot of the RHD model st35gm03n07 computed in the IONIC filter (top row) and in the K222 filter (bottom row). I used 20000 random triangles with a maximum triangle side extension of 40m (left column) and 100m (right column) as a function of their maximum side (long and short baseline are included). The closure phases are commonly not zero or

$\pm\pi$[15]. This is a clear signature of surface inhomogenities.

It is interesting to notice that the first large deviation from the circular symmetry is visible at about frequency 0.013 $R_\odot^{-1}$ (structures of $\sim$80 $R_\odot$, third lobe in the visibility curves, Fig. 8.14) for the IONIC filter, and at 0.02 cycles/$R_\odot$ (structures of $\sim$50 $R_\odot$, fourth lobe) where the closure phase become positive.
The closure phases at higher frequencies strongly deviates from the circular symmetry and the dispersion is more important in the H band. Above 0.043 cycles/$R_\odot$, the numerical resolution of RHD is attained (see Sect. 8.4.1) and the deviations correspond to structures smaller than 50 $R_\odot$.

Observing at higher spatial frequencies is important for the closure phases because they clearly deviate from the circular symmetry. The H band is a good target because the dispersion of the closure phases is large. This is only a first statistical approach. A forthcoming paper will compare these observables to the observation of α Ori in the H band (IONIC filter) by Haubois et al. (2006).

[15]the values zero or $\pm\pi$ are typical of point symmetric brightness distribution

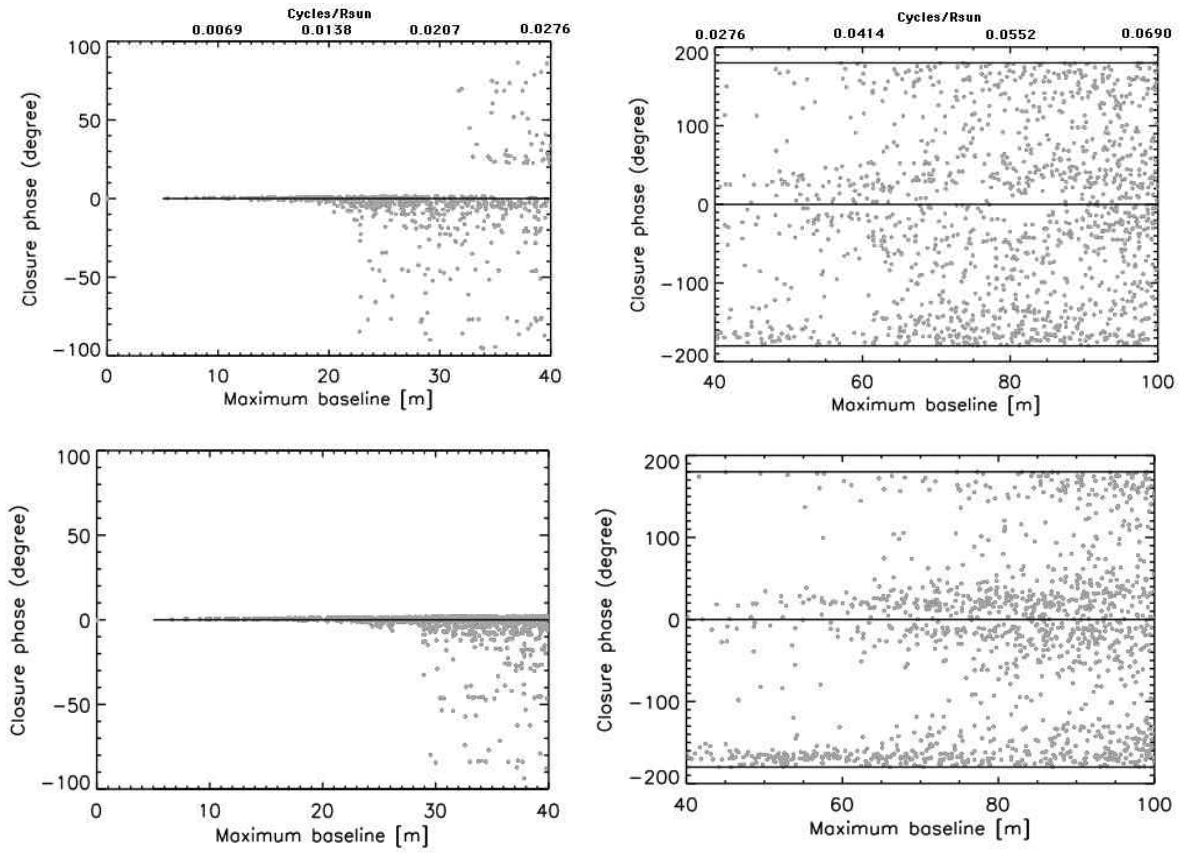

Figure 8.25: Scatter plot of closure phases of 20000 random baseline triangles with a maximum linear extension of 40m (left column) and 100m (right column) as a function of the maximum projected baseline (and cycles/$R_\odot$). The axisymmetric case is represented by the black line. *Top row:* IONIC filter centered at 1.64μm. *Bottom row:* K222 filter centered at 2.22μm.

8.5 Comparison with the observations

I start the comparison with the observations with the already published data in the K band for α Ori and μ Cep. Then, I will present the results of α Ori in the H band for a large set of data that cover spatial frequencies from the first to the fourth/fifth lobe.

8.5.1 α Ori in the K band

I compared the synthetic visibilities derived from the temporal and spatial evolution of the snapshots in the simulation st35gm03n07 (see Tab. 4.1) with the observation of α Ori by Perrin et al. (2004a) in the K band. The absolute model dimensions have been scaled to match on the interferometric observation in the continuum filter K222 (Fig. 8.4, top panel), and the resulting diameter is $\theta \sim 43.6$ mas at a distance of 179 pc. The interferometric data belong to the first, second and third lobes. I computed a large number on visibility curves and I found that the data are within the scatter due to the convection related surface structures (Chiavassa et al. 2008), the dotted lines in the Fig. 8.26.

Within this large number of visibility curves, I found that there are some calculated visibility curves that match all the observation points better than the uniform disk (with a diameter of 43.65 mas) or limb-darkened disk model (linear limb darkening law with a diameter of 43.64 mas and parameter 0.09 in Perrin et al. 2004a) do.
Fig. 8.26 shows an example. The best fit (χ^2=0.002) has been found performing the Levenberg-Marquardt least-squares minimization. The RHD simulation (solid line) is a great improvement over parametric models (UD model in dashed with χ^2=0.353 and the LD model in dotted-dashed with χ^2=0.382) for the interpretation of interferometric observations. The calculated visibility reproduces the observations points of the first second and third lobes with only one curve. There is one observed point in the first lobe at 24.5 arcsec^{-1} which is difficult to reproduce: in fact, adjustments on the absolute model dimensions of the star in order to fit this point, would lead to mismatch of the other observations at higher frequencies. However, the filter used (K222) for computing the maps is not exactly the same as the one used for these observations and this could affect the visibiltity curves or the calibration of the observed data may be wrong.
Since the interferometric data are reproduced by a RHD simulation, I can conclude that the surface of α Ori, in the K band, appears to be covered by convective cells of a typical size of 70-100 $R_\odot$ that contribute to the visibility at high frequencies (second and third lobes, see Sect. 8.4.3) and by cells of a typical size of $\sim$ 200 $R_\odot$ (first lobe, see Sect. 8.4.2). A more detailed analysis of α Ori surface, that will confirm this result in the H band, is reported in Sect. 8.5.3.

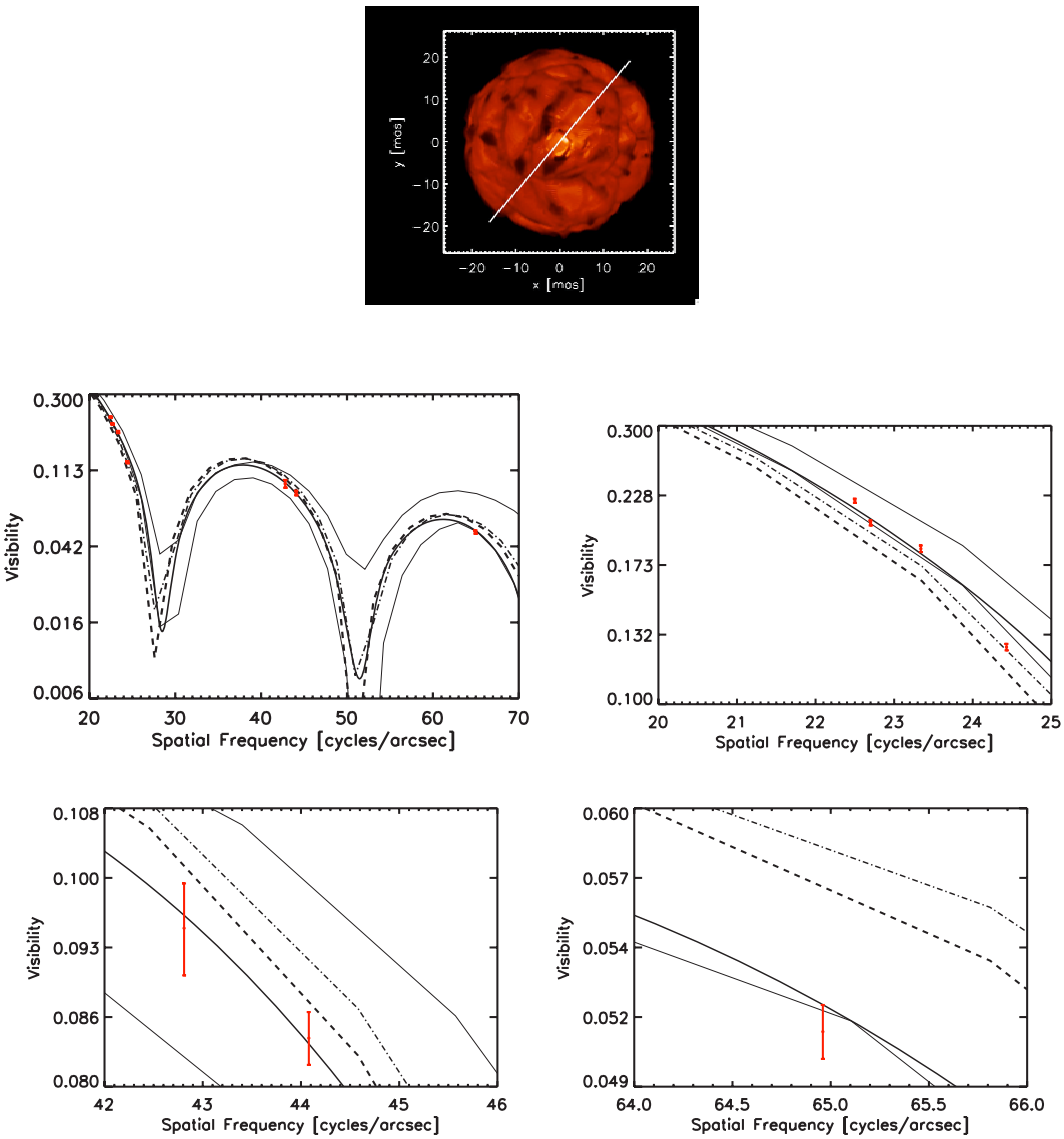

Figure 8.26: Comparison of the simulation described in the text with the α Ori observations (red dots) by Perrin et al. (2004a). *Top panel:* Map of the linear intensity in the K222-FLUOR filter (see Fig. 8.4, top panel). A scale is used within the range [0,150000] erg/s/cm^2/Å. The stellar parameters of this snapshot are: L = 93480.53 $L_\odot$, R = 832.72 $R_\odot$, T = 3496.71 K and log(g) = -0.34. The simulation has been scaled to an apparent diameter of 43.6 mas at a distance of 179 pc. The white line indicates the angle used for computing the visibility reported in the other panels. *Other panels:* the solid black line corresponds to the best fit visibility curve (thin solid lines are the minimum and maximum amplitude of variations of the visibilities), the dotted-dashed line is the limb-darkened (linear limb darkening law with a diameter of 43.64 mas and parameter 0.09) model and the dashed line the uniform disk (43.65 mas) model both introduced by Perrin. A logarithm scale is used.

8.5.2 μ Cep in FLUOR filters

I compared the synthetic visibilities derived from the temporal and spatial evolution of the snapshots in the simulation st35gm03n07 (see Tab. 4.1) with the observation of μ Cep by Perrin et al. (2005) in the four FLUOR filters (Fig. 8.27). The absolute model dimensions have been scaled to match the interferometric observation in the continuum filter K222, the apparent diameter is $\theta \sim 15.8$ mas at a distance of 490 pc.

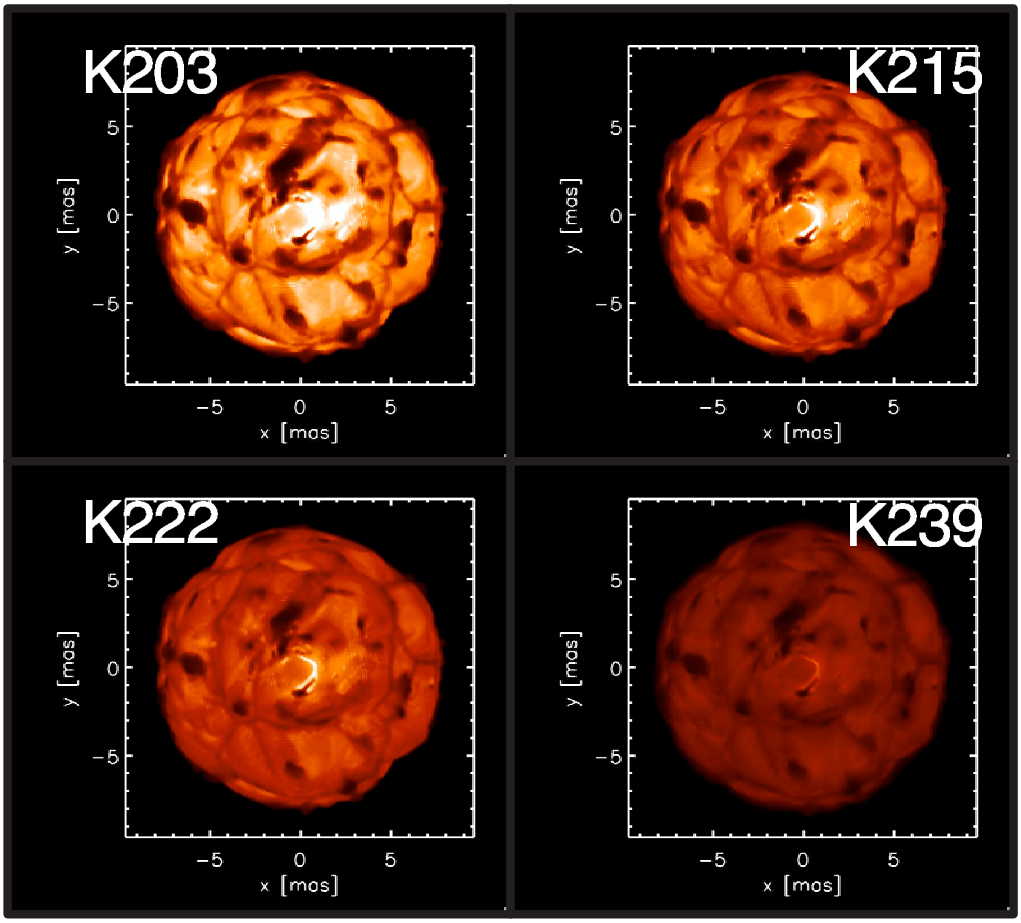

Figure 8.27: Maps of the linear intensity in the FLUOR filters (see Fig. 8.4, top panel). A temperature scale is used within the range [0,120000] erg/s/cm^2/Å. The stellar parameters of this snapshot are: L = 92490.43 L$_\odot$, R = 832.67 R$_\odot$, T = 3487.52 K and log(g) = -0.34. The simulation has been scaled to an apparent diameter of 15.8 mas at a distance of 490 pc.

Perrin et al. found that the observation points clearly indicate that the apparent radius of the star varies with the wavelength: the two continuum filters K215 and K222 gives the higher visibilities (ie., the smallest radius), while the K203 (mostly CN) and K239 (mostly CO) filters display visibilities corresponding to larger apparent sizes. In order to explain

the discrepancy, Perrin et al. used an ad-hoc geometrical model in which the photosphere is surrounded by an emissive and absorbing H_2O layer a few radii above the stellar surface.

I first try to reproduce the observed data with the three-dimensional model and for this purpose, I computed visibility curves from different angles for different snapshots and also for their temporal evolution (the reader must remember that there is not a clear distinction between the visibility fluctuations of spatial and temporal evolution, see Sect. 8.4.3). Fig. 8.28 shows that in the first lobe the visibility fluctuate ($<$10% with respect to the average visibility, see Sect. 8.4.2) and the dispersion depends on the large scale granule ($\sim$250 to $\sim$500 $R_\odot$). The are some discrepancies between the model and the data, and they are more evident in the edge filters (K203, top left; and K239, bottom right). For K203, the point at frequency $\sim$45 arcsec^{-1} corresponds to surface structures of $\sim$280 $R_\odot$. In the corresponding intensity map (Fig. 8.27, top left panel), only large scale granules are visible: if there were more cells with a typical size of $\sim$280 $R_\odot$ the visibility fluctuations could increase and the interferometric data could be reproduced. For K239, the points at $\sim$20 and 30 arcsec^{-1} correspond to structures of $\sim$500 and 350 $R_\odot$, respectively. In this case, in Fig. 8.27, K239 appear foggier than the other filters. The large scale granules are veiled by the contribution of CO lines. If the large cells would be more visible, the visibility fluctuations could increase.
In order to see if a different convection pattern would explain the data, I carried out a test using a different cube face of the RHD simulation with a different distribution of the convective cells. Even in this case the RHD model cannot explain the mismatched data. The three-dimensional model is not able to explain the μ Cep data in the first lobe with one single model.

In order to explain the discrepancies between the RHD model and the data, I have implemented an ah-hoc physical model characterized by an extension of the photosphere with a constant temperature and density. The whole star is surrounded by a shell with the real physical opacity derived from the input temperature and density. I have done this for the same snapshot as in (Fig. 8.27).
The MOLsphere input parameters are its temperature, density, and outer radius. The radius of the MOLsphere is equal $\sim$946 $R_\odot$ that corresponds to $\sim$9 mas at a distance of 490 pc (the radius of the star is 832.72 $R_\odot$, 7.91 mas). This value has been set enlarging the original radius with the same amount needed by the visibility curves to reproduce the data in the K239 filter.
The density is $\sim 1. \times 10^{-12}$ gr/cm^3 and the temperature is 1700 K, using these values the extinction coefficient of the MOLsphere is found interpolating into OPTIM3D opacity tables. The temperature and density has been found starting with an initial guess based on the equivalent width of water vapor lines at 12 μm (see Sect. 6.2.3) and by testing different values ranging from 1000 to 2000 K for temperature and 10^{-12} to 10^{-10} gr/cm^3 for density. Too high temperature (1800 - 2000 K, almost photospheric temperatures) or density (10^{-10} gr/cm^3) result into a entirely opaque surface in K203 (i.e., it becomes like an uniform disk). This could be verified with interferometric observations at higher frequencies than the first lobe: if the filter K203 in completely opaque, there would not be the signature of the convection on the visibility curves. This would suggest the existence

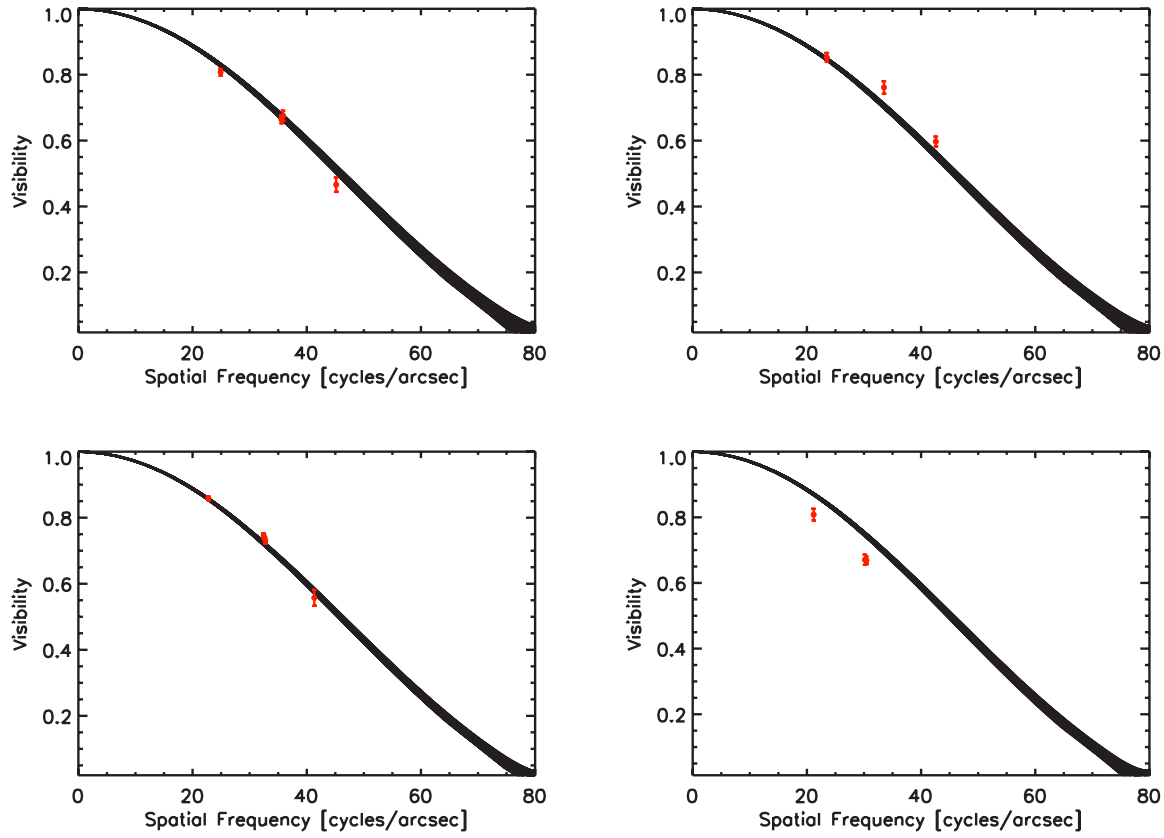

Figure 8.28: Visibilities as a function of spatial frequencies for the snapshot in Fig. 8.27 (36 angles with an step of 5°). Red dots are μ Cep observations by Perrin et al. (2005). The panels correspond to the FLUOR filters as described in Fig. 8.4: K203 top left panel, K215 top right, K222 bottom left and K239 bottom right.

of a MOLsphere with the parameters mentioned above.

Fig. 8.29 shows the ratio, at the stellar limb, between the MOLsphere model intensity profile and the not-extended model (Fig. 8.27) for each FLUOR filters. The intensity of the MOLsphere extension in K203, K215 and K222 filters are about a factor 1000 higher than the not-extended snapshot at ∼1.14 radius/$R_\star$ (i.e., the radius of the molsphere), this is due to the high temperature of 1700K used for the MOLsphere. In K239 filter the intensity increases of a factor 10.

I then computed the visibility curves for 36 angles with a step of 5° for the MOLsphere model.

Fig. 8.30 shows there is no improvement for reproducing larger apparent radius in K239 (data points at 20 and 30 cycles/arcsec) and K203 (data points at 45 cycles/arcsec). Something is still missing and the ad hoc models seem not to be able to reproduce the μ Cep interferometric data. The attempt I have carried out with the MOLsphere model was aimed to check if a larger apparent radius would have explain the data in K203 and

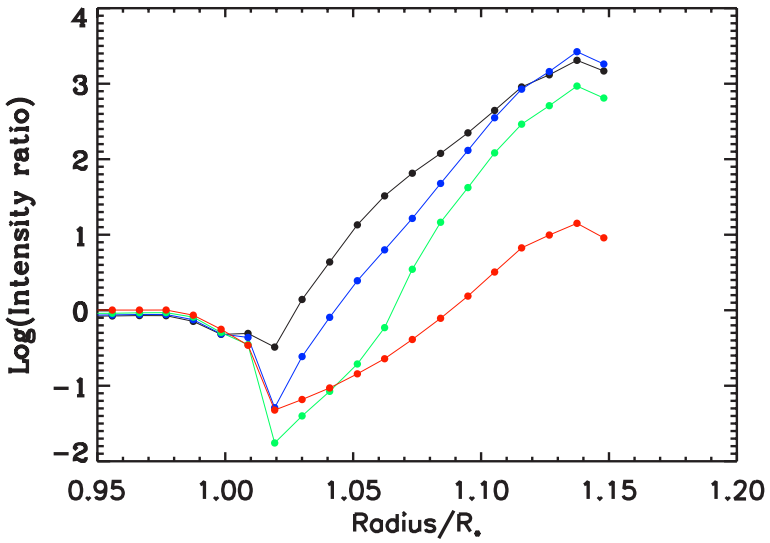

Figure 8.29: Ratio between the MOLsphere model intensity profile and the not-extended model (Fig. 8.27) intensity profile for each FLUOR filters (K203 is in black, K215 in blue, K222 in green and K239 in red). The radius of the MOLsphere is ∼1.14 radius/$R_\star$.

K239 simultaneously. The model was not able to reproduce the observations in K203 and K239. A more complicated MOLsphere model can be studied using an in-homogeneous distribution of the temperature/density for the extension of the atmosphere. However, I think that this will generate small patches of few $R_\odot$ that would contribute to the second, third and fourth lobe only (see Sect. 8.4.3).
In any case, this RHD simulation (st35gm03n07) is not able to explain the data. Another model with a larger surface gravity (e.g., log(g)=0. instead of -0.35 of the model used) and effective temperature of 3500 K should show more stellar granules with an horizontal size of ∼250 (Eq. 4.17) and maybe also the large cells change. In this case, the new configuration of the convection pattern will change visibility fluctuations. Simulations of with increased surface gravity are on-going and they will be tested soon.
The interferometric data are not enough to definitely affirm the presence or not of a MOLsphere around the RSG. Spectroscopic observations must be analyzed as well. This work is in progress and the point is to determine if the observed water vapor lines and OH lines at 12 μm in RSGs are formed in the photosphere or not. For this purpose, we use three-dimensional and one-dimensional models to reproduce the features.

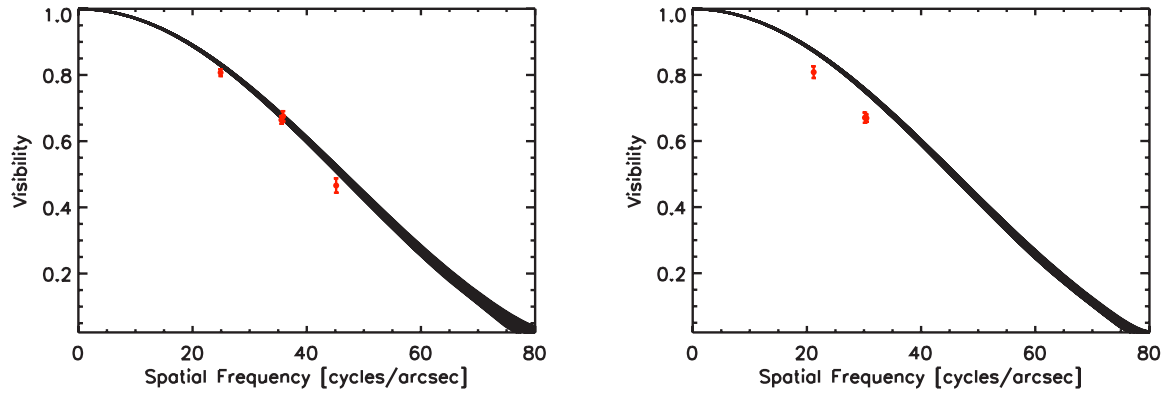

Figure 8.30: Visibilities as a function of spatial frequencies for the MOLsphere model (36 angles with an step of 5°). Only K203 (left panel) and K239 (right panel) are displayed. Red dots are μ Cep observations by Perrin et al. (2005).

8.5.3 α Ori in IONIC filter

I have also compared the RHD simulation to the α Ori interferometric data from Haubois et al. (2006). These observations have been taken with IOTA (Tab. 7.2) using the IONIC filter (Fig. 8.4). These data cover a large range of spatial frequencies between $\sim$ 12 to $\sim$ 95 arcsec^{-1} and the they have been collected within 10 days (less than the time-step of the RHD models, $\sim$23 days) between 7th October and 16th October 2005.
This comparison helps to find if RHD models do actually reproduce the visibility points at high arcsec^{-1} (second, third and fourth lobe). This region is crucial to identify the convection-related surface structures that affect the visibility curves (as shown in Sect. 8.4.3), and to establish the difference between RHD simulations and the parametric model (UD and limb-darkened disk) predictions.

In the following, I will use only the visibility obtained from the spatial evolution of six snapshots $\sim$ 230 day apart: in total I have considered 6 snapshots times 36 angles of the RHD simulation st35gm03n07 (the snapshots are taken within the sample presented in Fig. 4.7 and related Annex C). I did not analyze the temporal evolution of the intensity maps because the data have been collected within 10 daysand the time-step of the RHD simulation is $\sim$23 days. The absolute model dimensions have been scaled to match on the interferometric observation in the first lobe (the star has been scaled to a distance of 174.3 pc).
Fig. 8.31 displays the synthetic visibilities derived from one snapshot and for different angles (black curves) compared to the observations (red). It is not trivial to extract the information from this plot, however it is already obvious that the visibility dispersion due to convection-related surface structure, encompasses the observed data.

To quantify the comparison, I have performed a best-fit least-squares minimization (using Levenberg-Marquardt) within the large number of visibility curves presented in Fig. 8.31 and for the other snapshots. Fig. 8.32 shows the visibility curve that best fits the whole set of observed data with only one model. This visibility curve is one of the

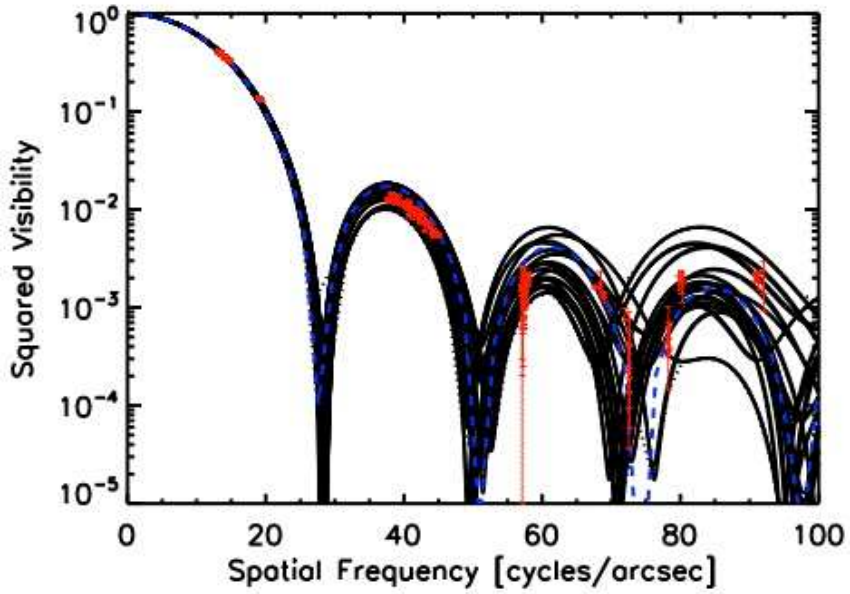

Figure 8.31: Predicted logarithmic squared visibilities (black) from the RHD simulation described in the text compared to the α Ori (red) interferometric data in the H band by Haubois et al. (2006) and Haubois private communication. Each curve corresponds to a different projected baseline angle, the angle-step is 5°. The simulation has been scaled to an apparent diameter of 44.8 mas, at a distance of 174.3 pc. The dashed blue line corresponds to a uniform disk model with a diameter of 43.65 mas.

visibilities in Fig. 8.31. Another example obtained from another snapshot is reported in Fig. 8.33.
The calculated visibility matches much better the observations than the uniform disk model (dashed blue line) in all lobes. All the observed points fall within the visibility fluctuations. The snapshot in Fig. 8.32 has smaller spatial visibility fluctuations (black dotted line) than the one in Fig. 8.33. This is a consequence of the fact that there are less small structures on the surface.

Since the synthetic maps have an random distribution of the surface structures, some observed points are not fitted because the exact condition of the observation are not matched. In order to reduce the dispersion of the observed data that derives from all the azimuth angles, I have packed the observations into 5° azimuth angle interval (the same angle step than for the calculated visibilities) and for each set I have searched for the visibility curve best-fit of the data. There are 16 sets between -55 and 50° azimuth (not all the 5° contains data). Some set contains data distributed at about the same frequency. I have chosen to report three examples of observation sets: the first contains data which span frequencies between the first and the second lobe (Fig. 8.34); the second example, observations between the first, second and third lobe (Fig. 8.35); and the third example, data in the the third and fourth lobe (Fig. 8.36). The best-fit has been found within visibility curves at different angles for the same time-step (luminosity = 92093.34 $L_{\odot}$, radius = 836.26 $R_{\odot}$, temperature = 3476.30 K and surface gravity = -0.34).

Fig. 8.34 and Fig. 8.35 show the good fit of the data (red) with synthetic visibility (black), especially at higher frequencies. In the first lobe, even if the observations falls outside the synthetic visibility, they are always within the visibility fluctuations (dotted lines). Only in Fig. 8.35 top right panel the observed data fall outside the visibility fluctuations amplitude at 14.2 arcsec^{-1}. Here, the observations error bars don't overlap and it difficult to say where the synthetic visibility should pass. This is not an isolated case in the observations. Possible explanations are: (i) the error bar are under-estimated (under studying by Haubois et al.), (ii) the visibility fluctuate of about 10% for azimuth angle step lower than 5°. The latter would mean that the distribution of the large cells or the apparent radius change abruptly within small angles (I don't see this in the simulation).

The conclusion is that the RHD simulations reproduce rather well the observations data of α Ori from lower to higher spatial frequencies with only one model. This is a great improvement with respect to the parametric models that apart from the first lobe, cannot explain the whole set of data.
For the first time, interferometric data have been collected above the second lobe, and they are crucial for a first investigation and interpretation of the convective pattern in RSGs. Since the interferometric data are reproduced by a RHD simulation, I can conclude that the surface of α Ori, in the H band, appears to be covered by convective cells of a typical size of 50-100 $R_\odot$ that contribute to the visibility at high frequencies (second, third and fourth lobe, see Sect. 8.4.3). This picture is also confirmed by the K band interferometric observations reported in Sect. 8.5.1 and by other interferometric observations (e.g., Young et al. 2000) and by spectroscopic observations (e.g., Josselin & Plez 2007 and Gray 2008). What is needed is a measure of the size distribution: the observations don't cover the frequencies $\sim$20-25 arcsec^{-1} that correspond to the signature of the large convective cell I see in the intensity maps. A systematic observation at different frequencies would tell if it is like the models predict.
Further comparison with the observed closure phases (on-going), observations with a temporal and spatial survey of RSG (VLTI-AMBER and future ESO applications, see Annex B) will definitely confirm the presence of large convective cells on the surface of RSG.

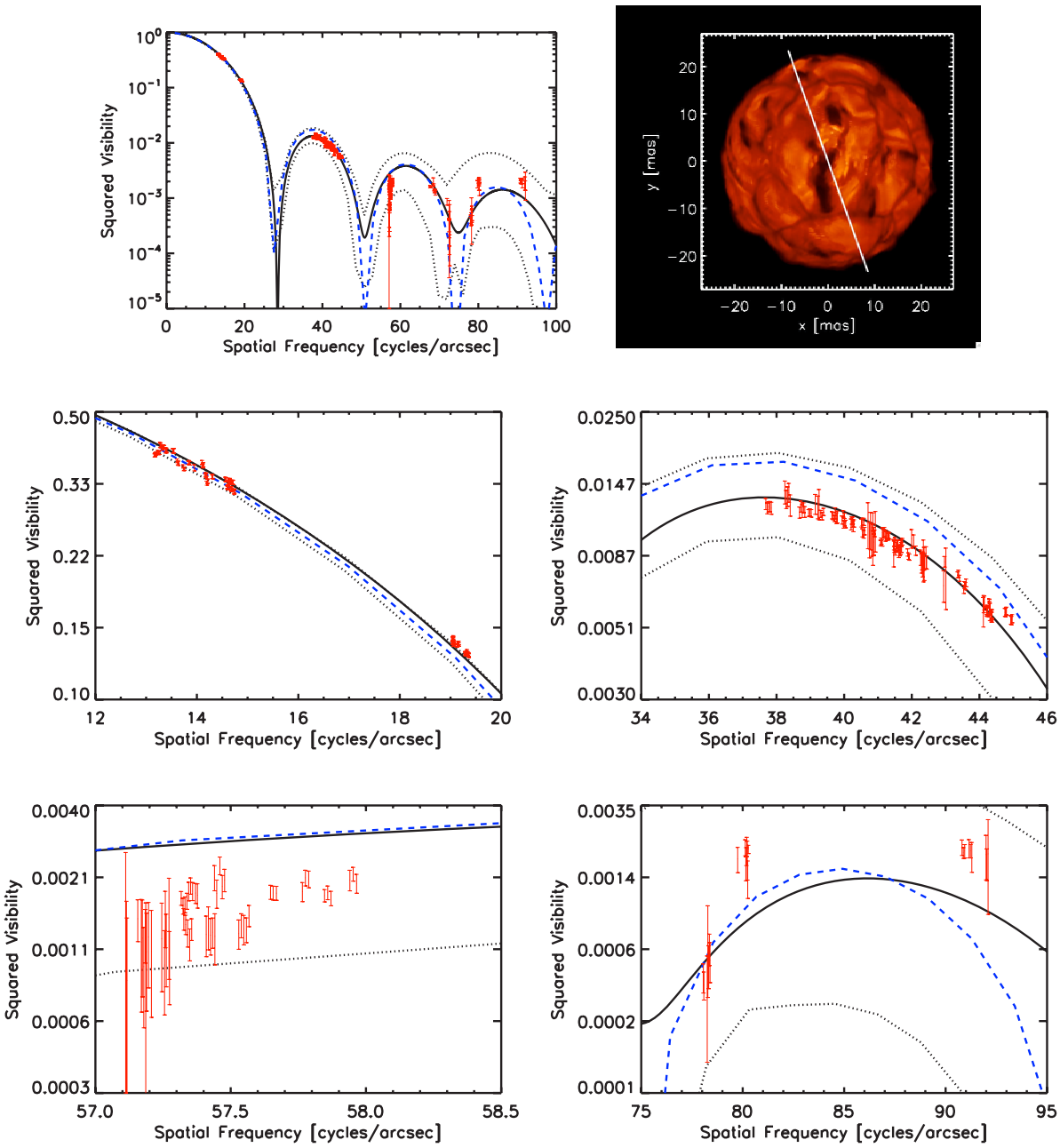

Figure 8.32: *Top right panel:* Map of the linear intensity in the IONIC filter (see Fig. 8.4, bottom panel). A scale is used within the range [0,310000] erg/s/cm^2/Å. The stellar parameters of this snapshot are: L = 96048.29 L$_\odot$, R = 836.77 R$_\odot$, T = 3511.95 K and log(g) = -0.34). The simulation has been scaled to an apparent diameter of 44.8 mas, at a distance of 174.3 pc. The white line shows the angle used to compute the visibility curves. *Top left panel:* best-fit of the predicted logarithmic squared visibility (black) from the sample in Fig. 8.31 compared to the observations in red. The other panels are enlargements. The blue dashed line is a uniform disk with a diameter of 43.65 mas. The dotted line are the maximum and minimum amplitude of the visibility fluctuations.

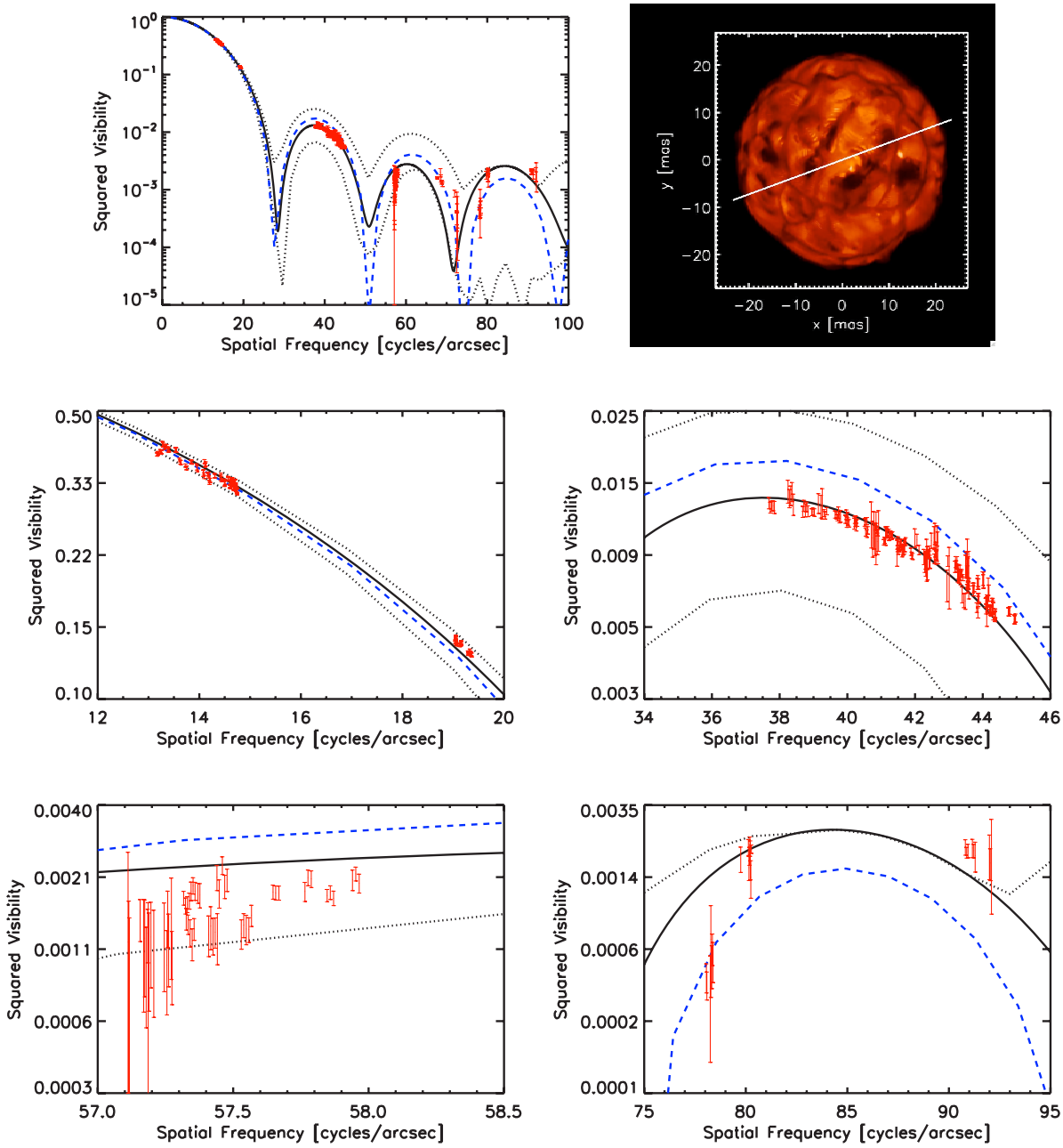

Figure 8.33: Same as in Fig. 8.32, with L = 93041.92 $L_\odot$, R = 834.44 $R_\odot$, T = 3489.01 K and log(g) = -0.34. The simulation has been scaled to an apparent diameter of 44.6 mas, at a distance of 174.3 pc.

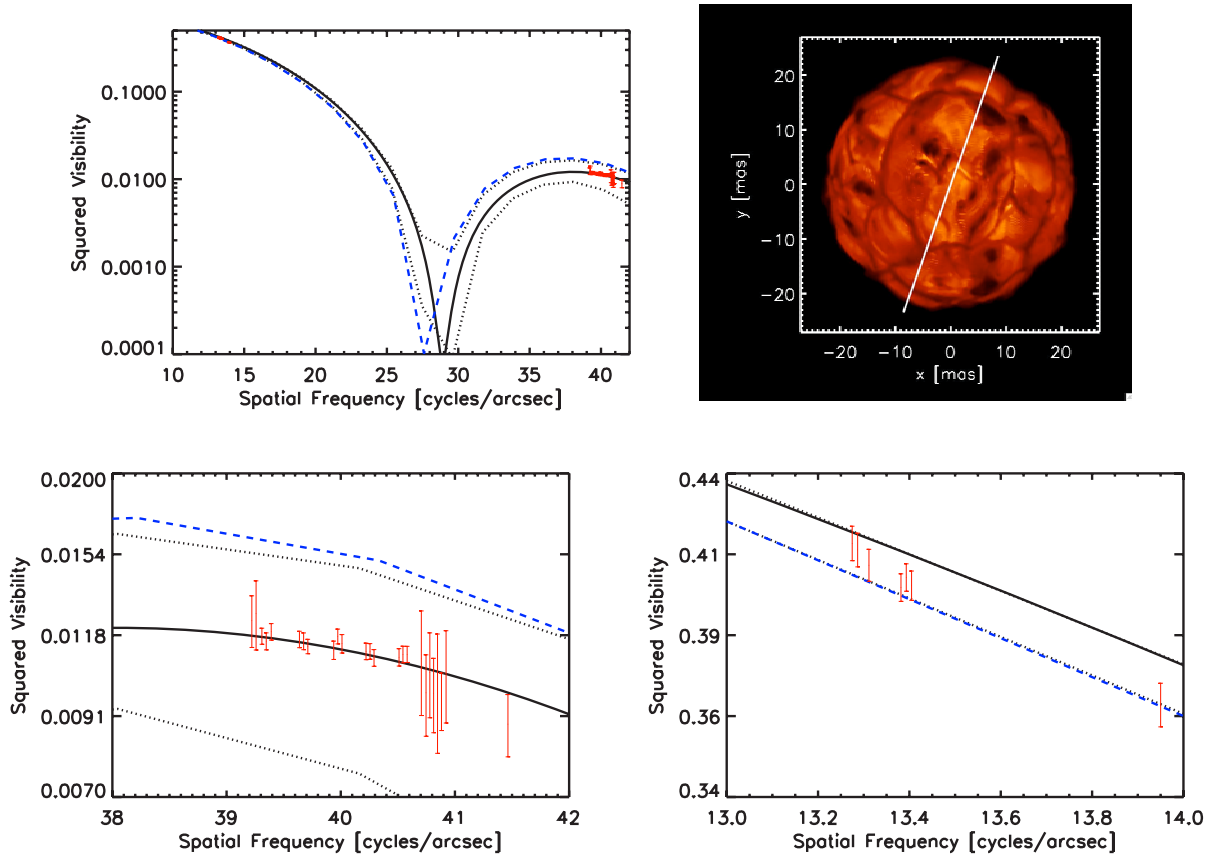

Figure 8.34: *Top right panel:* Map of the linear intensity in the IONIC filter (see Fig. 8.4, bottom panel). A scale is used within the range [0,310000] erg/s/cm^2/Å. The stellar parameter of this snapshot are: L = 92093.34 L$_\odot$, R = 836.26 R$_\odot$, T = 3476.30 K and log(g) = -0.34. The simulation has been scaled to an apparent diameter of 44.6 mas, at a distance of 174.3 pc. The white line shows the angle used to compute the visibility curves. *Other panels:* best-fit of the predicted logarithmic squared visibility curve (black) compared to one set of [-50.00, -45.00] azimuth from the observations in red (top left panel). The other panels are enlargements. The blue dashed line is a uniform disk with a diameter of 43.65 mas. The dotted lines are the maximum and minimum amplitude of the visibility fluctuations.

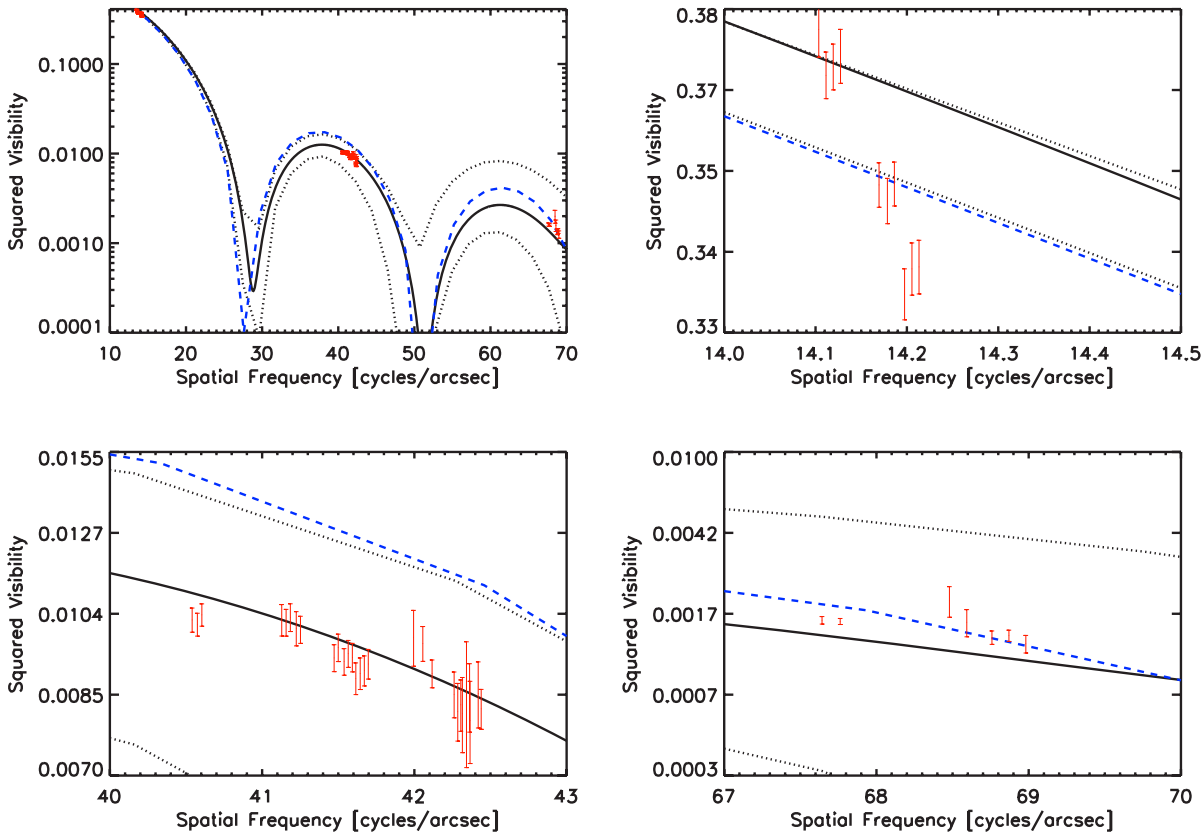

Figure 8.35: Best-fit of the predicted logarithmic squared visibility curve (black) compared to one set of [40.00, 45.00] azimuth from the observations in red (top left panel). The other panels are enlargements. The blue dashed line is a uniform disk with a diameter of 43.65 mas. The dotted lines are the maximum and minimum amplitude of the visibility fluctuations. The visibilities have been computed from the intensity map in Fig. 8.34 (top right panel).

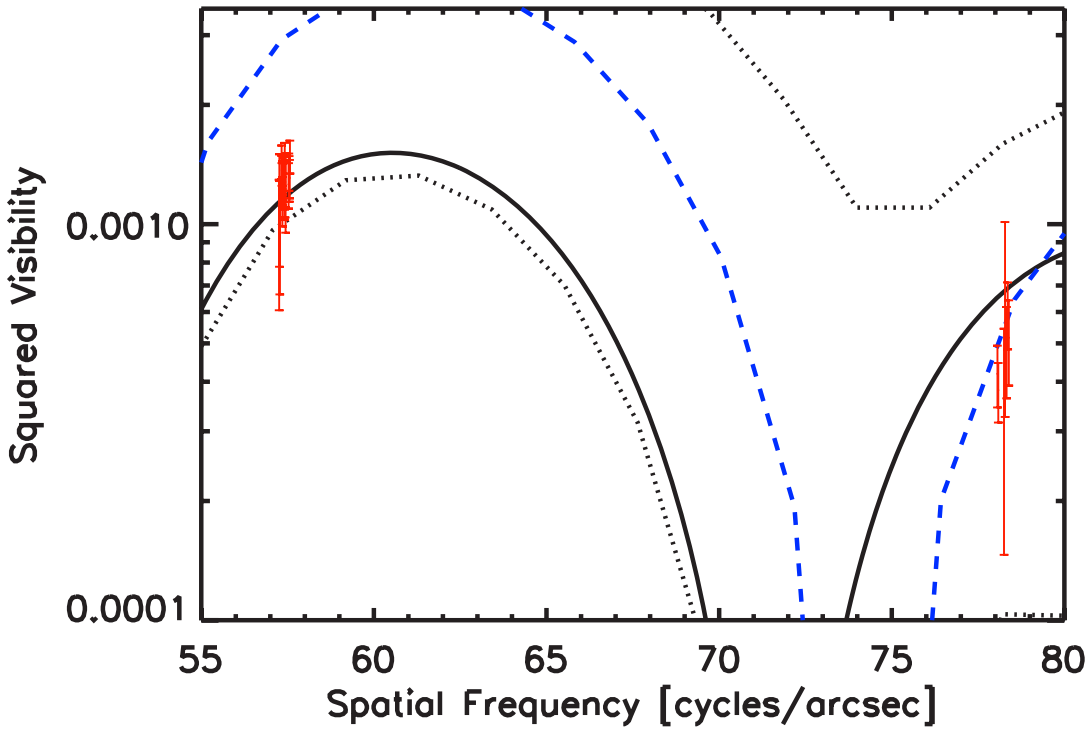

Figure 8.36: Best-fit of the predicted logarithmic squared visibility curve (black) compared to one one set of [5.00, 10.00] azimuth from the observations in red (top left panel). The other panels are enlargements. The blue dashed line is a uniform disk with a diameter of 43.65 mas. The dotted lines are the maximum and minimum amplitude of the visibility fluctuations. The visibilities have been computed from the intensity map in Fig. 8.34 (top right panel).

8.6 Science cases

I collaborated with the science case group for VSI (Malbet et al. 2008 and in Appendix A).
VSI (VLTI Spectro-Imager) is a next generation instrument at VLTI. It will provide the ESO-community with spectrally-resolved near-infrared (J, K, H bands) images at angular resolution down to 1.1 milliarcsecond, and spectral resolution up to R=12000. Targets as faint as K=13 will be imaged without requiring a brighter nearby reference star. The instrument will combine up to 6 beams from UTs or ATs telescopes and it will be capable to measure 15 visibility points simultaneously (5 times faster than AMBER with only 3 beams and 3 visibility points).

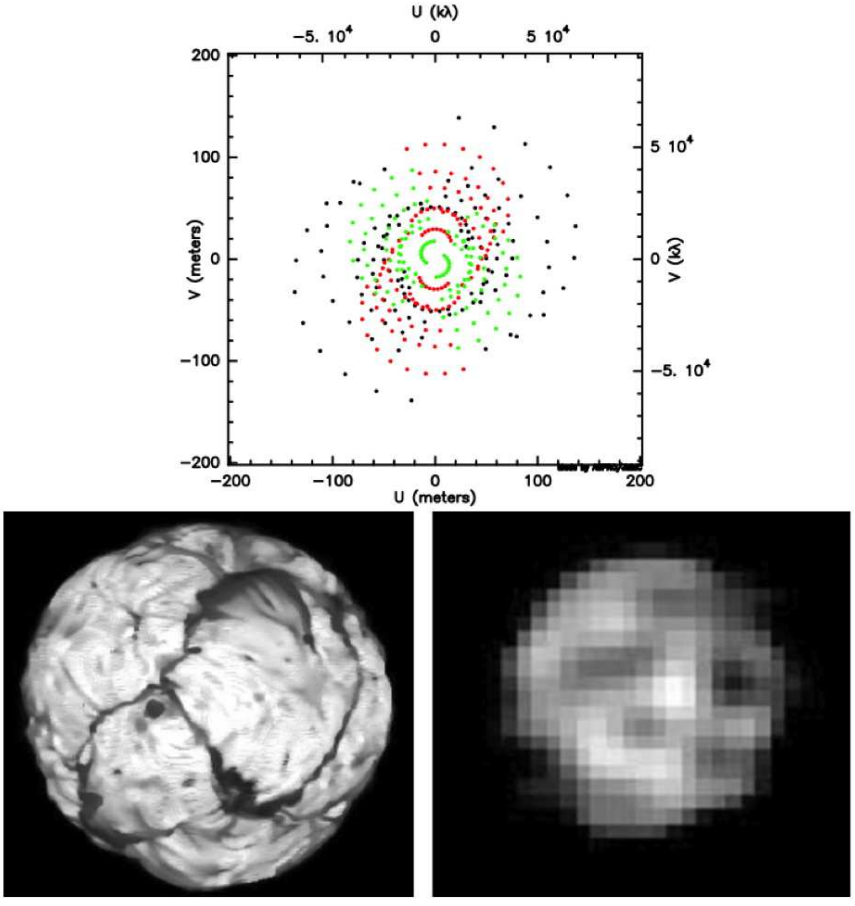

Figure 8.37: Image reconstruction using VSI. *Bottom left:* synthetic image of a snapshot of st35gm03n08 (Tab. 4.1) at 2.2 μ m; *top panel:* Fourier plan coverture of 4 ATs for three nights (Earth rotation); *bottom right:* reconstructed image, image courtesy of Mercedes Esteves Filho (Centro de Astrofisica da Universidade do Porto).

I also furnished some intensity maps for the MATISSE (Multi Aperture Mid-Infrared SpectroScopic Experiment), that is also a next generation instrument at VLTI developed by a European consortium (http://www.oca.eu/matisse/). This instruments will measure visibility curves and closure phases in the N band (8-13 μm, the same as MIDI), L (3-5 μm) and M (4.6-5.5 μm) with an angular resolution of 4.5 milliarcsecond in the L band and 10 milliarcsecond in the N band. In addition, the instrument will cover a spectral resolution from R=30 to R$\sim$1000. MATISSE is the successor of MIDI and in particular it will capable to measure the closure phases and to combine four beams simultaneously.

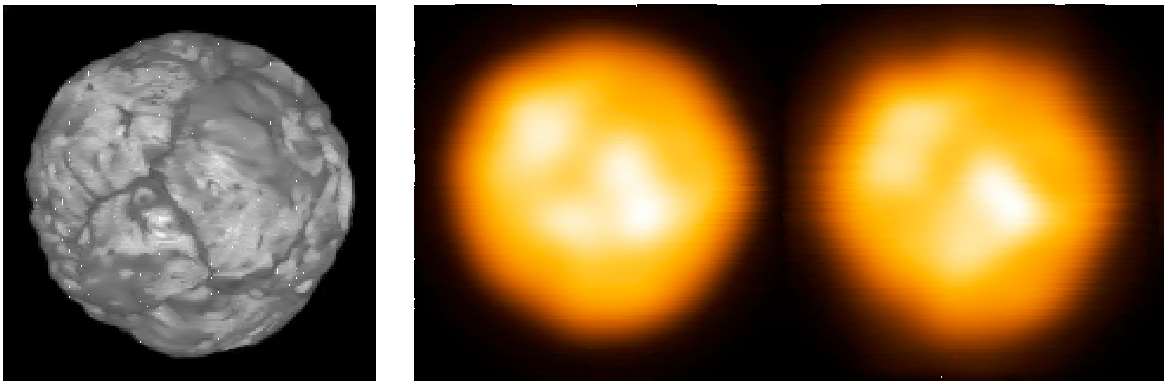

Figure 8.38: Image reconstruction using MATISSE. *Left pannel:* synthetic image of a snapshot of st35gm03n08 in the L band (Tab. 4.1); *Central and right panels:* reconstructed image, based on the simulated MATISSE observations. The target is considered to be at the position of the star Bet Gru (α=22:42:40, δ=46:53:04, size: 28 mas). In the central panel the image with an ideal 150m telescope; in the right panel recontructed image with 3x4 ATs (baseline=150m). For more details see Doc. No. VLT-TRE-MAT-15860-4325.

Among the science cases for VSI and MATISSE, the imaging of stellar surfaces is a important one because they will provide a powerful means to resolve the surface granulation of stars like the RSGs. VSI and MATISSE, as an imaging device, is of strong interest to study various specific features such as temperature contrast, typical sizes of surface inhomogeneities (at different depths in the atmosphere), surface intensity contrast and to detect their variability with time. These observations will strongly constrain RHD simulations at different wavelengths.